

GEOLOGICAL MAPPING AND FULL POLARIMETRIC SAR
ANALYSIS OF SILICA SAND DISTRIBUTION ON THE
NORTHERN COASTLINE OF RUPAT ISLAND, INDONESIA

(インドネシア・ルパ島北部沿岸におけるケイ砂分布の地質マ
ッピングと全偏波合成開口レーダ解析)

January 2017

HUSNUL KAUSARIAN

Graduate School of Advanced Integration Science

CHIBA UNIVERSITY

(千葉大学審査学位論文)

GEOLOGICAL MAPPING AND FULL POLARIMETRIC SAR
ANALYSIS OF SILICA SAND DISTRIBUTION ON THE
NORTHERN COASTLINE OF RUPAT ISLAND, INDONESIA

(インドネシア・ルパ島北部沿岸におけるケイ砂分布の地質マ
ッピングと全偏波合成開口レーダ解析)

January 2017

HUSNUL KAUSARIAN

Graduate School of Advanced Integration Science

CHIBA UNIVERSITY

ABSTRACT

Rupat Island is a part of Bengkalis district, Riau province, Indonesia. There is silica sand distribution on the northern coastline of this island. The silica sand is not originated by this island bedrock, it comes by the Malacca Strait sea-flow. Silica sand was used as the base material for solar cell panel even as the base material for the oil and gas industry as the filter and also used for the glass and ceramic industries. From the ground survey and microscopic photograph testing, silica sand sample shows homogeneous characteristic with a white colour, which has the grain size in round shape and the grain size is almost same size. Laboratory tests using the XRF (X-Ray Fluorescence) and XRD (X-Ray Diffraction) shows the silica compound (SiO_2) has a high percentage above 95%. Two adjacent ALOS PALSAR Full polarimetry data were used to analyse the distribution of silica sand by developed the technique to identify the silica sand and estimate the thickness of silica sand distribution using the dielectric constant value. The result from the ground survey validation and SAR data analysis shows the technique is successful in identifying and estimating the thickness for the silica sand distribution.

ABSTRACT (JAPANESE)

インドネシア・リアウ州のルパ島北部沿岸にはケイ砂が広く分布している。この地域の地層形成過程によると、このケイ砂地層はルパ島の岩盤由来ではなく、マラッカ海峡の海流で流着したものである。ケイ砂は太陽電池パネルやガラスをはじめ、多くの工業用途に用いられている。本研究では、同島から採取したケイ砂サンプルの物理特性を調べるとともに、合成開口レーダ (SAR) センサであるALOS PALSARの偏波解析 (PoISAR) によりケイ砂分布のマッピングを行った。採取試料の顕微鏡観察から、ケイ砂粒は白色で、粒径が比較的均一な球形に近い形状であること、また、蛍光X線とX線回折の測定から、二酸化ケイ素が体積比95%以上を占めていることが分かった。さらに、誘電率情報を用いたPoISAR解析では、偏波散乱分解 (表面散乱, 体積散乱, ダブルバウンス, ヘリクス) を行ってケイ砂分布と厚みの分類を行った。その結果、表面散乱による分類結果がもっと高い精度を示すことが明らかになった。

CONTENTS

1	INTRODUCTION.....	1
2	STUDY AREA.....	6
	2.1 Rupert Island.....	6
	2.2 Geological Condition.....	7
3	METHODOLOGY.....	11
	3.1 Geological Mapping, Sample Validation on the Site Observation and Laboratory Test.....	11
	3.2 Synthetic Aperture Radar (SAR) Data and Sample Properties Analysis.....	18
4	RESULT AND DISCUSSION.....	29
	4.1 Distribution and the Origin of Silica Sand on the Northern Coastline of Rupert Island.....	32
	4.2 The Percentage of Silica Compound.....	38
	4.3 Result of Synthetic Aperture Radar (SAR) Data and Sample Analysis.....	44
	4.4 Thickness estimation of silica sand layer.....	56
5	CONCLUSION AND FUTURE PLANNING.....	70
	5.1 Conclusion.....	70
	5.2 Contribution.....	72
	5.3 Future Planning.....	73
6	REFERENCES.....	75
7	APPENDICES.....	81

LIST OF TABLES

Table 1.1	The Common Content of Sand in Nature.....	2
Table 3.1	The Specification of X-RF Instrumentation.....	16
Table 3.2	The Specification of X-RD Instrumentation.....	17
Table 3.3	Specification of ALOS PALSAR Full-Polarimetry Data of Rupat Island.....	18
Table 4.1	X-RF Result of Silica Percentages of the Silica Sand Samples from Northern Part of Rupat Island.....	39
Table 4.2	Table of backscattering coefficient Value from ALOS PALSAR and field, average error and average ratio.....	45
Table 4.3	Table of dielectric constant of sample, backscattering coefficient Value from ALOS PALSAR and field, average error, average ratio and silica sand layer thickness estimation from study area at northern coastline of Rupat Island.....	59

LIST OF FIGURES

Figure 1.1	Location of Study Area on the Province of Riau, Indonesia. (Insert is the Map of Indonesia).....	3
Figure 2.1	The Geological Map of Rupert Island.....	6
Figure 2.2	Silica Sand Distribution Field Observation Points on the Northern Coastline of Rupert Island.....	7
Figure 2.3	The Aerial Photograph of Silica Sand Distribution on the Northern Coastline of Rupert Island	7
Figure 2.4	Geological Structure of Central Sumatera Basin.....	8
Figure 2.5	Lithological and Sedimentary Stratigraphy of Central Sumatera Basin.....	9
Figure 3.1	Beting Aceh Observation Location on the Northern Coastline of Rupert Island.....	12
Figure 3.2	Tanjung Api Observation Location on the Northern Coastline of Rupert Island.....	12
Figure 3.3	Teluk Rhu Observation Location on the Northern Coastline of Rupert Island.....	13
Figure 3.4	Tanjung Punai Observation Location on the Northern Coastline of Rupert Island.....	13
Figure 3.5	Tanjung Lapin Observation Location on the Northern Coastline of Rupert Island.....	14
Figure 3.6	Two-dimensional analysis model for composing three layers media; the infinite length of air, the thickness ξS of silica sand layer, and infinite depth of Peat layer as the bedrock. (b) The equivalent circuit of the model.....	20
Figure 3.7	Geo-rectification Process of PALSAR Image in This Study...	25
Figure 3.8	The Image Processing Step (a. Before Correction, b. Geometry Correction Process, c. Geo-rectified Image, d. Validation by Projected to the Google Earth).....	26

Figure 3.9	The Measurement Process to Calculate Dielectric Constant Value (A: Setting the parameter; frequency range, and number point of counting, B-D: Calibration of the air, probe, and water temperature, E: Cleaning the dielectric probe kit, F: Measuring the sample).....	28
Figure 4.1	The Sample of Silica Sand from Beting Aceh Area	29
Figure 4.2	The Sample of Silica Sand from Tanjung Api Area.....	30
Figure 4.3	The Sample of Silica Sand from Teluk Rhu Area.....	30
Figure 4.4	The Sample of Silica Sand from Tanjung Punai Area.....	31
Figure 4.5	The Sample of Silica Sand from from Tanjung Lapin Area...	31
Figure 4.6	The Estimation of Silica Sand Distribution from the field observation.....	32
Figure 4.7	Waterway Flows of Malacca Strait as a Sediment Transport Agent for the Silica Sand Sedimentation.....	33
Figure 4.8	Grain Size from Microscopic Photograph of Silica Sand Samples from Beting Aceh Location.....	35
Figure 4.9	Grain Size from Microscopic Photograph of Silica Sand Samples from Tanjung Api Location.....	35
Figure 4.10	Grain Size from Microscopic Photograph of Silica Sand Samples from Teluk Rhu Location.....	36
Figure 4.11	Grain Size from Microscopic Photograph of Silica Sand Samples from Tanjung Punai Location.....	36
Figure 4.12	Grain Size from Microscopic Photograph of Silica Sand Samples from Tanjung Lapin Location.....	37
Figure 4.13	Silica Sand Samples from the Northern Coastline of Rupert Island.....	37
Figure 4.14	The Profile of X-Ray Diffraction from Beting Aceh (BA) Sample.....	40

Figure 4.15	The Profile of X-Ray Diffraction from Tanjung Api (TAp) Sample.....	41
Figure 4.16	The Profile of X-Ray Diffraction from Teluk Rhu (TRh) Sample.....	42
Figure 4.17	The Profile of X-Ray Diffraction from Tanjung Punai (TPn) Sample.....	43
Figure 4.18	The Profile of X-Ray Diffraction from Tanjung Lapin (TLp) Sample.....	44
Figure 4.19	The relationship graph between backscattering coefficient from satellite and field observations.....	46
Figure 4.20	Freeman-Durdeen Decomposition from Two Adjacent Scenes of Rupert Island.....	47
Figure 4.21	Yamaguchi Decomposition from Two Adjacent Scenes of Rupert Island.....	48
Figure 4.22	Flat condition from the Distribution of silica sand on the northern coastline of Rupert Island, (a) Beting Aceh Location, (b) Tanjung Api Location.....	49
Figure 4.23	Above: Google Earth's Image as the Reference Shown the Silica Sand as White Color along the Northern Coastline of Rupert Island.....	51
Figure 4.24	Double Bounce Scattering Decomposition on the Northern Coastline of Rupert Island ((a) Beting Aceh location, (b): Tanjung Api location).....	51
Figure 4.25	Volume Scattering Decomposition on the Northern Coastline of Rupert Island ((a) Beting Aceh location, (b): Tanjung Api location).....	52
Figure 4.26	Surface Scattering Decomposition on the Northern Coastline of Rupert Island ((a) Beting Aceh location, (b): Tanjung Api location).....	52

Figure 4.27	Helix Scattering Decomposition on the Northern Coastline of Rupat Island ((a) Beting Aceh location, (b): Tanjung Api location).....	53
Figure 4.28	Value of Backscattering Coefficient from Polarimetric Decomposition of Double Bounce Scattering on the Northern Coastline of Rupat Island ((a) Beting Aceh location, (b): Tanjung Api location).....	54
Figure 4.29	Value of Backscattering Coefficient from Polarimetric Decomposition of Volume Scattering on the Northern Coastline of Rupat Island ((a) Beting Aceh location, (b): Tanjung Api location).....	54
Figure 4.30	Value of Backscattering Coefficient from Polarimetric Decomposition of Surface Scattering on the Northern Coastline of Rupat Island ((a) Beting Aceh location, (b): Tanjung Api location).....	55
Figure 4.31	Value of Backscattering Coefficient from Polarimetric Decomposition of Helix Scattering on the Northern Coastline of Rupat Island ((a) Beting Aceh location, (b): Tanjung Api location).....	55
Figure 4.32	Relationship between silica sand layer thickness and backscattering coefficient.....	57
Figure 4.33	Dielectric Constant Value of Silica Sand Sample no. 1 in the Beting Aceh Area.....	60
Figure 4.34	Dielectric Constant Value of Silica Sand Sample no. 2 in the Beting Aceh Area.....	60
Figure 4.35	Dielectric Constant Value of Silica Sand Sample no. 3 in the Beting Aceh Area.....	61
Figure 4.36	Dielectric Constant Value of Silica Sand Sample no. 4 in the Tanjung Api Area.....	61

Figure 4.37	Dielectric Constant Value of Silica Sand Sample no. 5 in the Tanjung Api Area.....	62
Figure 4.38	Dielectric Constant Value of Silica Sand Sample no. 6 in the Tanjung Api Area.....	62
Figure 4.39	Dielectric Constant Value of Silica Sand Sample no. 7 in the Teluk Rhu Area.....	63
Figure 4.40	Dielectric Constant Value of Silica Sand Sample no. 8 in the Teluk Rhu Area.....	63
Figure 4.41	Dielectric Constant Value of Silica Sand Sample no. 9 in the Teluk Rhu Area.....	64
Figure 4.42	Dielectric Constant Value of Silica Sand Sample no. 10 in the Tanjung Punai Area.....	64
Figure 4.43	Dielectric Constant Value of Silica Sand Sample no. 11 in the Tanjung Punai Area.....	65
Figure 4.44	Dielectric Constant Value of Silica Sand Sample no. 12 in the Tanjung Punai Area.....	65
Figure 4.45	Dielectric Constant Value of Silica Sand Sample no. 13 in the Tanjung Lapin Area.....	66
Figure 4.46	Dielectric Constant Value of Silica Sand Sample no. 14 in the Tanjung Lapin Area.....	66
Figure 4.47	Dielectric Constant Value of Silica Sand Sample no. 15 in the Tanjung Lapin Area.....	67
Figure 4.48	Dielectric Constant Value of Silica Sand Sample no. 16 in the Tanjung Lapin Area.....	67
Figure 4.49	Relationship between silica sand thickness from satellite and field measurement.....	69

LIST OF ABBREVIATIONS AND ACRONYMS

mm	Millimeter
SiO ₂	Silicon dioxide
kg/m ³	Kilogram per meter cubic
C	Celsius
Qh	Recent Surface Sediment
Qp	Older Surface Sediment
N	North
E	East
S	South
W	West
km ²	Kilometre square
km	Kilometre
NW-SE	Northwest – southeast
m.a	Million age
BA	Beting Aceh
TAp	Tanjung Api
TRh	Teluk Rhu
TPn	Tanjung Punai
TLp	Tanjung Lapin
XRF	X-Ray Fluorescence
XRD	X-Ray Diffraction

ALOS	Advanced Land Observing Satellite
PALSAR	The Phased Array type L-band Synthetic Aperture Radar
TiO ₂	Titanium dioxide
Al ₂ O ₃	Aluminum oxide
Fe ₂ O ₃	ferric oxide
MnO	Manganese (II) oxide
MgO	Magnesium oxide
CaO	Calcium oxide
Na ₂ O	Sodium oxide
K ₂ O	Potassium oxide
P ₂ O ₅	Diphosphorus pentoxide
SAR	Synthetic Aperture Radar
cm	Centimeter
GHz	Gigahertz
L-Band	Low-frequency Band
Az	Azimuth resolution
Ra	Range resolution
P 1.1	Polarimetry level 1.1 product
NE	Noise Equivalent
dB	Decibel
Z_S	The effective impedance of silica sand layer
Z_P	The parallel of peat layer impedance
Z_{TS}	The total input of impedance

E	Electromagnetic wave
θ_i	Incident angle
ξ_s	The thickness of silica sand layer
γ_s	The constant propagation
ϵ_{rs}	The dielectric constant complex
μ_{rs}	The specific permeability complex
θ_{ts}	The transmission angle
λ_s	The wavelength
j	Imaginary number
Z_0	The impedance wave in air or free space
Γ	Reflectivity coefficient
$\sigma^0(f)$	The backscattering coefficient from field
$\sigma^0(s)$	Backscattering coefficient from satellite
CF	The conversion factor
\bar{e}	The average error
$\bar{\alpha}$	The average ratio
$f_{s,d,v,c}$	Expansion coefficients
P	Power
$[C]$	Covariance matrix
$[T]$	Coherency
S	Scattering matrix
%	Percentage
bdl	Below detection limit

L.O.I	Lost on ignition
CPS	Count per second
DblScat	Double Bounce Scattering
VolScat	Volume scattering
SrfScat	Surface scattering
HlxScat	Helix scattering

1 INTRODUCTION

Silica sand is one of the minerals which relatively abundant in Indonesia. This is possible due to Indonesia geological condition, which is almost as acidic igneous rock that formed mineral source [1]. Silica sand is acidic weathering of igneous rocks such as granite or other igneous rock containing major mineral like quartz. The quality of silica sand in Indonesia is quite varied, depending on the process and the influence of mineral genesis impurities formed during sedimentation processes involved.

In the nature, silica sand can be found with varied of grain size, fine grain size (< 0.06 mm) located far from source rock and (> 2 mm) located not far from the source rock [2] (Table 1.1). Crystalline of quartz (SiO_2) mostly in white colour, with a white shine and polished glass. With un-perfect parts and pieces that are not flat (conchoidal), mineral crystal has a hexagonal bipyramid prism shape, with the specific gravity 2.65 kg/m^3 and hardness is 7 (Mohs scale) [3], [4] and it has outstanding durability in the process of abrasion/erosion. Melt at a temperature of $1,710^\circ \text{C}$ [5]. When experience rapid cooling, will provide an amorphous texture.

This mineral was used in the industry such as building materials and the main ingredient in the design of interior/exterior [6], [7] as well as materials for household need. As the followed material, silica sand used as the printed materials in the foundry [8], [9], [10], refractory materials and as filler in the mining and petroleum industry [11], especially when performing drilling activities.

Table 1.1 The Common Content of Sand in Nature.

Compound/Mineral	Weight Percentage
SiO ₂	55,30-99,87%
Fe ₂ O ₃	0,01-9,14%
Al ₂ O ₃	0,01-18,00%
TiO ₂	0,01-0,49%
CaO	0,01-3,24%
MgO	0,01-0,26%
K ₂ O	0,01-17.00%

Silica sand hands an important role for the industry, especially in base materials either as the primary or auxiliary raw materials. As the main raw material, silica sand used for cement industry, glass, bottles and glassware [8]. While the auxiliary raw materials used in petroleum industry [11] and others. Silica sand is one of the minerals which relatively abundant in Indonesia. This is possible due to the geological condition of Indonesia, which had the almost acidic igneous rock that formed minerals source [1]. One of the areas that have been abundant with silica sand sedimentation is Rupert Island (Figure 1.1), Bengkalis district, Riau province, Indonesia. Silica sand in this island distributes on the north coastline area only.

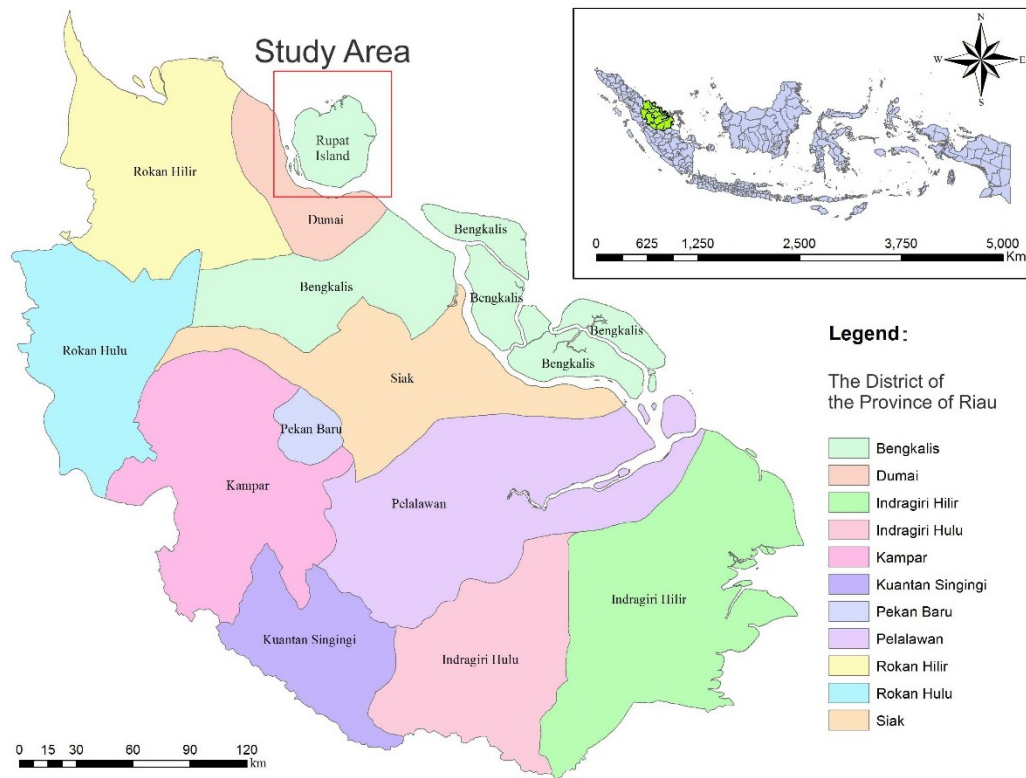


Figure 1.1. Location of Study Area on the Province of Riau, Indonesia. (Insert is the Map of Indonesia).

Rupat Island (Figure 1.1) is a part of Bengkalis district which located in front of Dumai City, Indonesia. Rupat Island has a breadth of 1,500 km². Geological setting of this island consists of Recent Surface Sediment formation (Qh) and Older Surface Sediment formation (Qp). The high silica content accumulated with other compounds in the silica sand found on the Bukit Pelintung area which is located nearby from Rupat Island [12].

The purpose of this study is to know the percentage, the origin and the distribution of silica sand in Rupat Island also to conduct an inventory and determine the potential (characterization and utilization) of silica sand resources in the Rupat Island, Bengkalis district, Riau province, Indonesia.

2 STUDY AREA

2.1 Rupert Island

Rupert Island is a part of Bengkalis district located in front of Dumai city. The island has a breadth of 1,500 km². There are two subdistricts in this island, first is Rupert subdistrict with the capital city is Batu Panjang and the second is Rupert Utara subdistrict with Tanjung Medang as the capital city.

Rupert Subdistrict has an area of 894.35 km². Rupert subdistrict has a large number of villages located on the coast area. Only Kebumen Parit village located is on the mainland, and Pangkalan Nyirih village and Hutan Panjang located at the watershed.

The largest village on the Rupert subdistrict is Makeruh village with the total area is 100 km², or 16.88% of the total Rupert subdistrict entirely. And the smallest village is Sukarjo Mesim village with the total area is 26 km² or 2.91% of entirely.

Villages with the furthest straight distance from the capital of Rupert subdistrict is Makeruh village with the straight distance is 78 km. And the shortest distance is Batu Panjang village as the capital district.

Rupert subdistrict has 12 villages, they are Tanjung Kapal, Batu Panjang, Terkul, Pergam, Sei Cingam, Teluk Lecah, Pangkalan Nyirih, Hutan Panjang, Makeruh, Parit Kebumen, Sukarjo Mesim, and Darul Alam. Rupert subdistrict located at 1° 41'12" North until 2° 00' North and 101° 23'19" East until 101° 47'14" East. Rupert subdistrict boundaries are as follows:

- Northern: Rupert Utara subdistrict.
- Southern: The city of Dumai.
- Western: The District of Rokan Hilir.
- Eastern: Strait of Malacca.

The subdistrict of Rupert Utara located at 0° 55'24" North until 2° 7'41" North and 101° 25'43" East until 101° 47'14" East. Based on data from the Rupert Utara subdistrict, the total area of Rupert Utara subdistrict is 628.50 km², with the largest village is the village of Titi Akar with the total area is 300 km², or by 47.73% of the total area of Rupert Utara subdistrict. The smallest village is Tanjung Punak with an area 66 km² or 10.50% of the total area.

Village with straight farthest distance from the capital of Rupert Utara is Titi Akar Village with straight distance of 25 km. And the shortest distance is Tanjung Medang as the capital of North Rupert subdistrict. Rupert Utara subdistrict has boundaries as below:

- Northern: Strait of Malacca.
- Southern: Rupert subdistrict.
- Western: The district of Rokan Hilir.
- Eastern: Strait of Malacca

2.2 Geological Condition

The location of Rupert Island is 1°41'12" N - 2°7'41" N and 101°23'19" E - 101°47'14" E with the total area about 1,500 km². Rupert Island is divided into 2 subdistricts, the first subdistrict is Rupert with Batu Panjang as the capital and the second subdistrict is Rupert Utara with Tanjung Medang as the capital.

Rupert Island has two main formations [13], [14], [15] which are Recent Surface Sediment formation (Qh) and Older Surface Sediment formation (Qp). Old Superficial Deposit formation (Qp) consisting of clay, silt, clay, gravel and remains of plants. Young Superficial Deposit formation (Qh) consisting of clay, silt, gravel

slippery, remains of plants and peat bogs. The formations aged from recent age. Silica sand was brought by Malacca Strait stream as the sediment transportation agent. Silica sand distributes only on the northern coastline of this island (Figure 2.1), aerial photograph for the observation point can be seen in Figure 2.2 and the field observation shows in Figure 2.3.

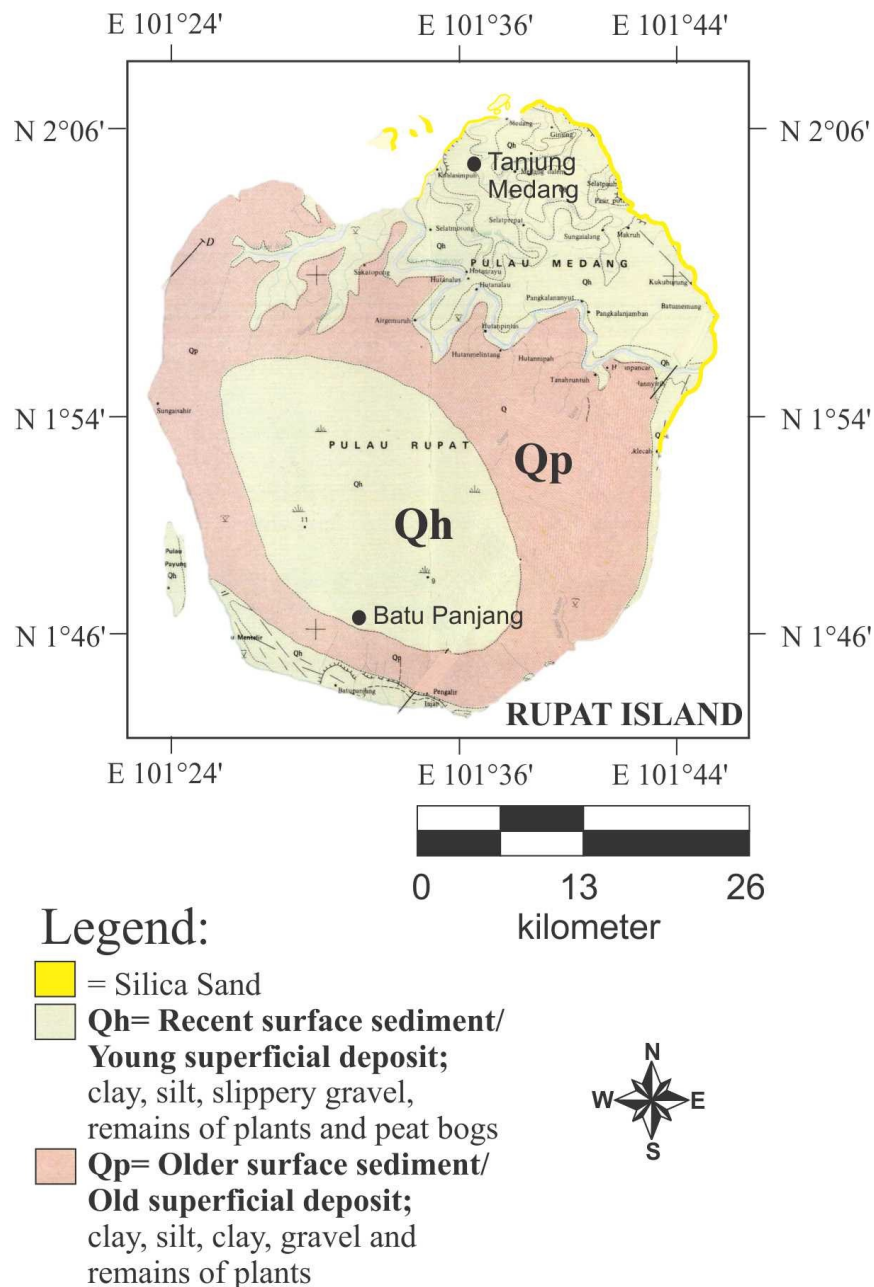


Figure 2.1. The Geological Map of Rupert Island.

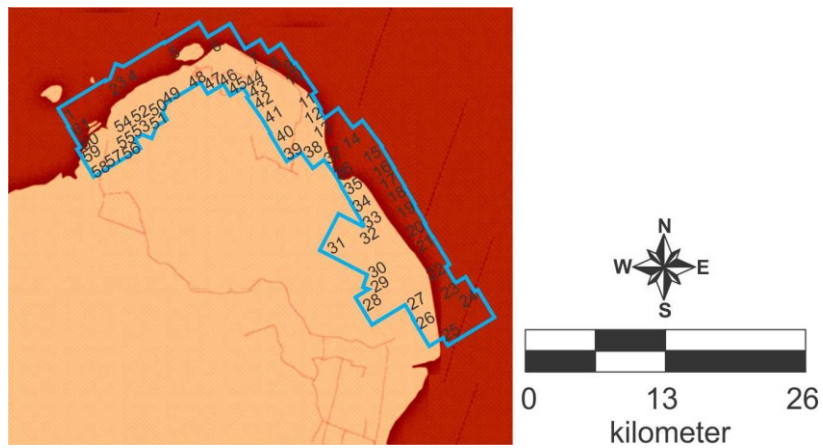


Figure 2.2. Silica Sand Distribution Field Observation Points on the Northern Coastline of Rupat Island.

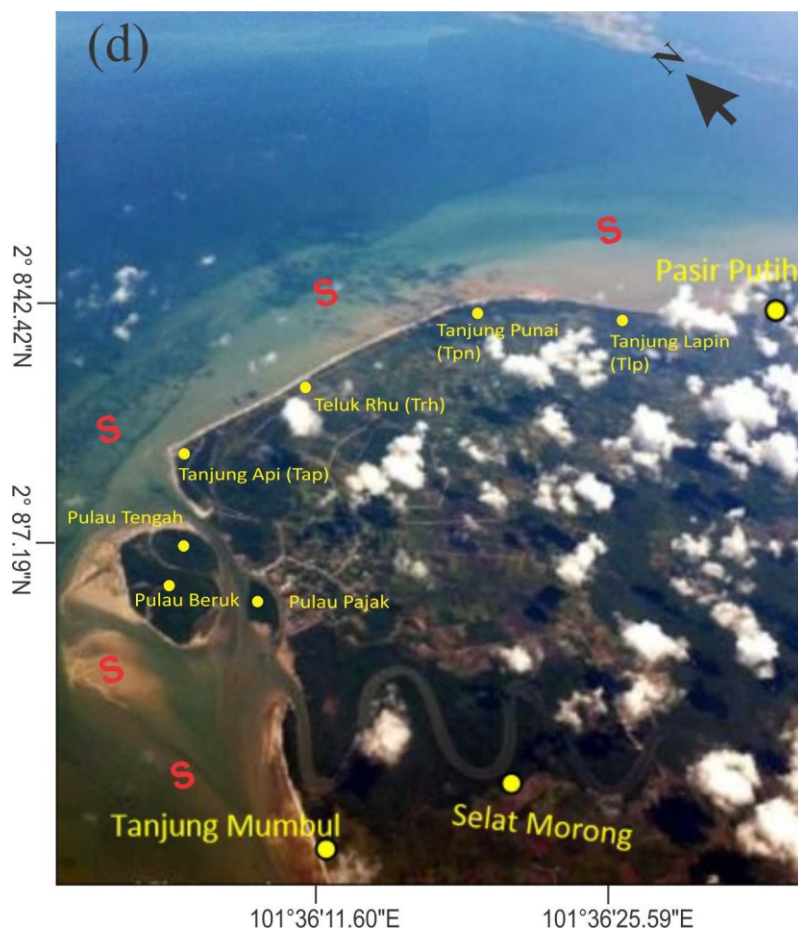


Figure 2.3 The Aerial Photograph of Silica Sand Distribution on the Northern Coastline of Rupat Island.

Rupat Island located in the north of Central Sumatra Basin and directly opposite the straits of Malacca [16]. The geological structure of the northern part of Central Sumatra Basin was developing at the time of Neogen and asymmetrical shape that led northwest-southeast (NW-SE) which is a pattern of young structure (Figure 2.4). The deepest part lies in the southwest part and sloping toward to the northeast. It is because of the appearance fracture faults in the base of basin that is generally half graben shaped. The bedrock of the northern part of Central Sumatra Basin is Quartzite Terrane, also called Mallaca Terrane, consists of quartzite, crystalline limestone, schist and shale with aged 295 m.a and 112-122 m.a, 150 m.a, respectively. This bedrock intruded by granitic pluton and granodioritic with Jura age. This group is found in the north to the northeast of coastal plain and Rupat Island has quartzite as its bedrock.

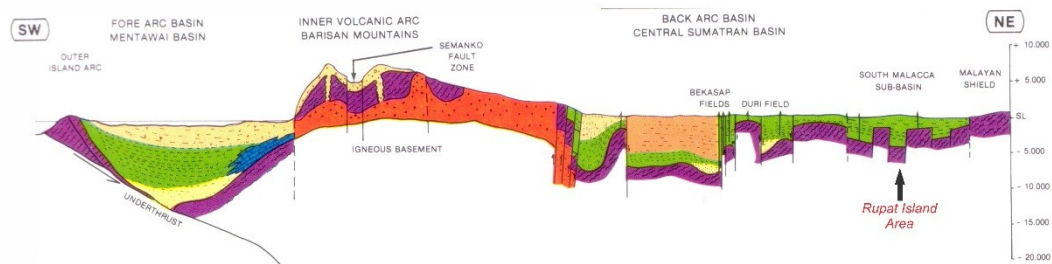


Figure 2.4. Geological Structure of Central Sumatera Basin.

Rupat Island is part of the Telisa formation. This formation is deposited as the repetition filled with Bekasap and Duri formations on the southwest and northeast, respectively [17]. In some places also found parallel deposition with those formations. This formation started from early Miocene to middle Miocene consists of a succession of sedimentary rocks dominated by shale with calcareous siltstone inserted with grey colour, brown and sometimes encountered with limestone (Figure 2.5).

The depositional environment for this formation started from neritic to non-marine [18]. One event that is quite important in Central Sumatra Basin is the emergence of igneous intrusion and extrusion aged on the middle Miocene (12-17 m.a) shortly

after a hiatus of Duri. The composition of intrusive rocks shows the depositional environment of the Back-arc Basin [17].

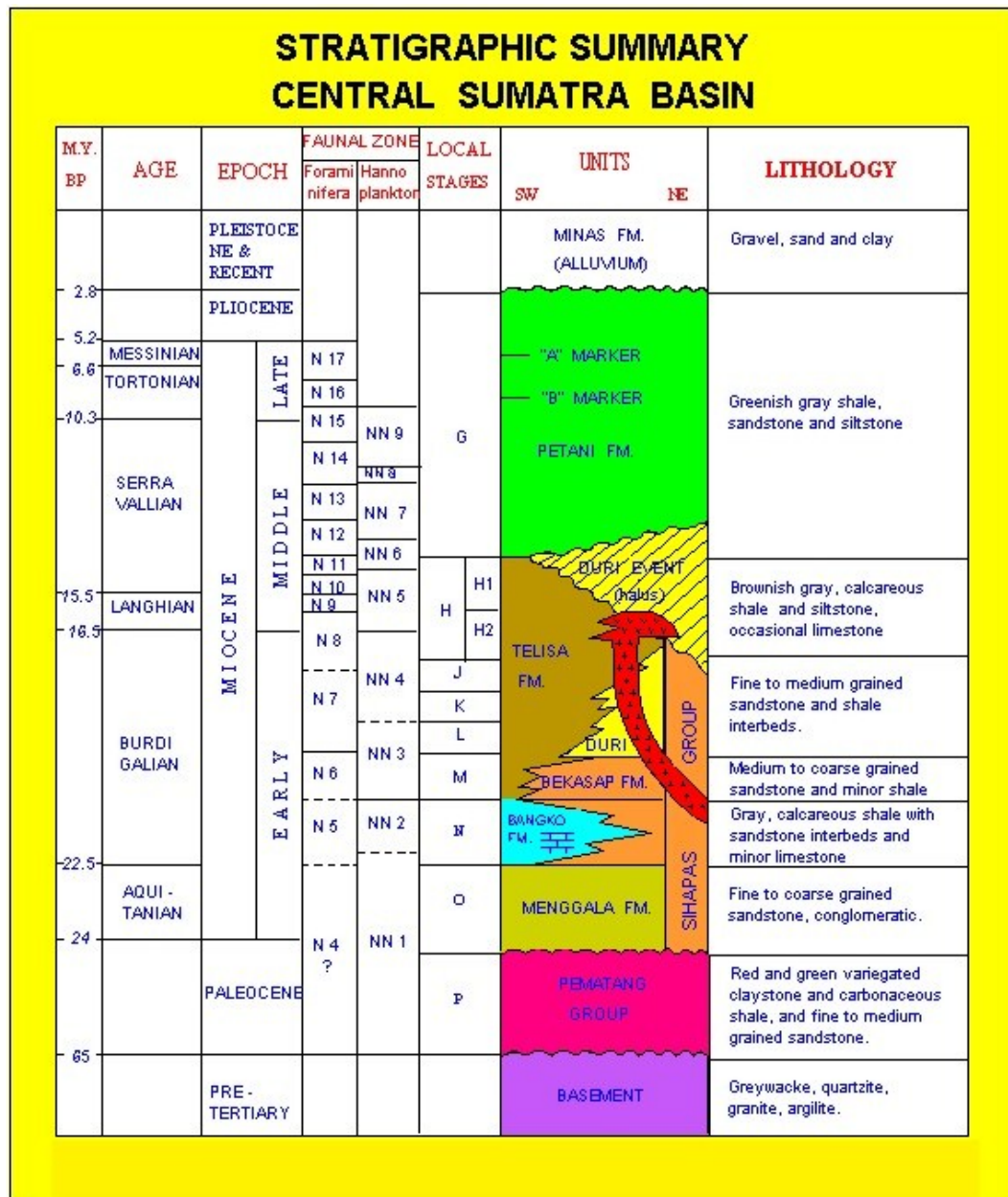


Figure 2.5. Lithological and Sedimentary Stratigraphy of Central Sumatera Basin.

The upper part of Rupert Island is composed of two formations; they are and Older Surface Sediment formation (Qp) and Recent Surface Sediment formation (Qh). Old Superficial Deposit formation (Qp) consisting of clay, silt, clay, gravel and

remains of plants. The second formation is Young Superficial Deposit (Qh) with clay, silt, gravel slippery, remains of plants and peat bogs as the composition of this formation. These formations are the recent age. The northern part of Rupert Island facing the Malacca Strait and rich with sand sediment reserve. The southern of this island facing Dumai City, coastal beach had more material with rich of mud sediment.

3 METHODOLOGY

3.1 Geological Mapping, Sample Validation on the Site Observation and Laboratory Test

3.1.1 Geological mapping

This study covering the plotting of observation points, the observation of sand outcrops, sampling and the laboratory analysis. Observation on the field at Rupert Utara subdistrict (northern part of Rupert Island) started in the area along the coastline location, these areas are: Tanjung Mumbul, Pulau Simpur, Pulau Kemunting, Pulau Babi, Beting Aceh, Pulau Pajak, Pulau Beruk, Pulau Tengah, Tanjung Medang, Teluk Rhu, Tanjung Punai, Tanjung Lapin, Pasir Putih. Based on observation on the field, there are five main observation locations were chosen as the represented study area along the northern coastline of Rupert Island, there are; Beting Aceh (BA) (Figure 3.1), Tanjung Api (TAp) (Figure 3.2), Teluk Rhu (TRh) (Figure 3.3), Tanjung Punai (TPn) (Figure 3.4) and Tanjung Lapin (TLp) (Figure 3.5). Sand sampling was conducted. The samples were collected from those areas.

The laboratory test was conducted to get the content of minerals in these samples. The laboratory test was used using X-Ray Fluorescence (XRF) and X-Ray Diffraction (XRD) to get that information. The microscopic photograph also used to know the shape of the fragment/grain of the mineral's composition. Study site covering the plotting of 16 observation points (see

Figure 2.2) as the geological mapping, sand sampling and testing in the laboratory.



Figure 3.1. Beting Aceh Observation Location on the Northern Coastline of Rupert Island.



Figure 3.2. Tanjung Api Observation Location on the Northern Coastline of Rupert Island.



Figure 3.3. Teluk Rhu Observation Location on the Northern Coastline of Rupert Island.



Figure 3.4. Tanjung Punai Observation Location on the Northern Coastline of Rupert Island.



Figure 3.5. Tanjung Lapin Observation Location on the Northern Coastline of Rupert Island.

Observation on the field on the northern coastline of Rupert Island started with these areas: Tanjung Mumbul, Pulau Simpbur, Pulau Kemunting, Pulau Babi, Beting Aceh, Pulau Pajak, Pulau Beruk, Pulau Tengah, Tanjung Medang, Teluk Rhu, Tanjung Punai, Tanjung Lapin, Pasir Putih. Based on observation on the field, there are 16 observation locations with five main locations where samples collected in these areas. The areas are Beting Aceh (BA), Tanjung Api (TAp), Teluk Rhu (TRh), Tanjung Punai (TPn) and Tanjung Lapin (TLp). The samples were collected during the dry season to be suitable with the same season when ALOS PALSAR data we used. Field observation and data collection were conducted in August 2014.

3.1.2 Sample validation on the site observation

Figure 2.3 also shown some study areas and silica sand distribution by an aerial photograph. Silica sand sampling was conducted using field collection such as excavation. All sample from the observation location shows the color of the sand is virtually white and homogeneous from the field observation that

has been done in this study area. It gave suggestion that the silica sand composition in this region had nearly the same silica content.

3.1.2 Laboratory test

The determination of silica percentage content and the compound of mineral properties, laboratory testing was used for the sand samples obtained from the field survey. The chemical analysis is needed to get the types of compounds/elements, the physical properties and the percentage content of the compounds/elements.

3.1.2.1 X-Ray Fluorescence (X-RF)

The laboratory test was conducted to get the content of minerals in these samples. X-Ray Fluorescence (X-RF) was used to get mineral's content information. The microscopic photograph also used to know the shape and size of the fragment/grain of the mineral's composition. X-RF (X-Ray Fluorescence) shows the result of silica sand samples contain of minerals which are SiO_2 (Silicon dioxide), TiO_2 (Titanium dioxide), Al_2O_3 (Aluminum oxide), Fe_2O_3 (ferric oxide), MnO (Manganese (II) oxide), MgO (Magnesium oxide), CaO (Calcium oxide), Na_2O (Sodium oxide), K_2O (Potassium oxide) and P_2O_5 (diphosphorus pentoxide). X-RF test were used to get compound/mineral percentage content for 5 main locations (Beting Aceh, Tanjung Api, Teluk Rhu, Tanjung Punai and Tanjung Lapin).

X-RF instrumentation used is X-RF PANalytical Epsilon 3 with specification as mentioned in Table 3.1.

3.1.2.2 X-Ray Diffraction (X-RD)

X-ray diffraction is one method to characterize an important raw material. X-ray diffraction method is used to obtain information material's crystal structure of metal and alloys, minerals, inorganic compounds, polymers,

organic materials, superconductors, crystal orientation, crystal type, grain size, lattice constants and others.

XRD characterization aims to determine the crystal system. X-ray diffraction method may explain the lattice parameters, the type of structure, a different arrangement of atoms in the crystal, the imperfections in the crystal orientation, grains, and size.

X-RD instrumentation used is Anchor Scan Parameters with specification as mentioned in Table 3.2.

Table 3.1. The Specification of X-RF Instrumentation.

Sample handling	X-ray tube	Detector	Software options
10-position removable sample changer	Metal-ceramic side window	Typically 135 eV	Stratos
Accommodates 25 to 52 mm diameter samples	50 micrometer thin window (Be)	8 micrometer thin window (Be)	Omnian
Spinner included	Software controlled, max. Voltage 50 kV, max. 1 mA, max. 9W	High-resolution silicon drift	FingerPrint

Table 3.2. The Specification of X-RD Instrumentation (*source:*
<http://www.panalytical.com/XPert3-Powder.htm>).

Explanation	Remark
Type of sample	Powder
Comment	Configuration=Reflection-Transmission Spinner, Owner=User-1, Creation date=9/5/2012 12:30:22 PM Goniometer=PW3050/60 (Theta/Theta); Minimum step size 2Theta:0.001; Minimum step size Omega:0.001 Sample stage=Reflection-Transmission Spinner PW3064/60; Minimum step size Phi:0.1 Diffractometer system=XPERT-PRO Measurement program=C:\PANalytical\Data Collector\Programs\program 1.xrdmp, Identifier={3CAD73EF-6481-4028-A7F8- 1C8E894F7CD6}
Operator	User
Raw Data Origin	XRD measurement (*.XRDML)
Scan Axis	Gonio
Start Position [$^{\circ}$ 2Th.]	10.0181
End Position [$^{\circ}$ 2Th.]	99.9781
Step Size [$^{\circ}$ 2Th.]	0.0260
Scan Step Time [s]	7.1400
Scan Type	Continuous
PSD Mode	Scanning
PSD Length [$^{\circ}$ 2Th.]	3.35
Offset [$^{\circ}$ 2Th.]	0.0000
Divergence Slit Type	Fixed
Divergence Slit Size [$^{\circ}$]	0.8709
Specimen Length [mm]	10.00
Measurement	25.00
Temperature [$^{\circ}$ C]	
Anode Material	Cu
K-Alpha1 [\AA]	1.54060
K-Alpha2 [\AA]	1.54443
K-Beta [\AA]	1.39225
K-A2 / K-A1 Ratio	0.50000
Generator Settings	30 mA, 40 kV
Diffractometer Type	0000000011130968
Diffractometer Number	0

Goniometer Radius [mm]	240.00
Distance Focus- Divergent Slit [mm]	100.00
Incident Beam Monochromator	No
Spinning	Yes

3.2 Synthetic Aperture Radar (SAR) Data and Sample Properties Analysis

3.2.1 Synthetic Aperture Radar (SAR) data analysis

In this study, we used two adjacent scenes of ALOS PALSAR full-polarimetry data (Table 3.3), the first full polarimetry ALOS PALSAR scene acquired on May 16, 2010, and the second were acquired on April 03, 2011. Acquired data was geocoded using orbit information. SAR observation performs in the slant or squint condition, the image was distorted from geometrically and radiometrically [19], [20], [21]. Meanwhile, the pixel height cannot be retrieved directly even when orbital data are accurate. As chosen study area is along the coastline with no significant topography, terrain correction was not performed [22], [23], [24].

Backscattering coefficient, polarization analysis method and scattered waves model from different types of surface soil were developed [25], [26], [27]. This method introduced calculation of backscattering coefficient as the relation with the electrical properties of the object for using the impedance characteristic of the surface roughness.

From the ground survey measurement and for simplifying the analysis, the surface roughness impact on the scattered waves was ignored, where the ground survey or field measurements showed the surface roughness was extremely shorter than the L-band wavelength (23.5 cm) [28], [29].

Table 3.3. Specification of ALOS PALSAR Full-Polarimetry Data of Rupat Island.

Configuration	Quadpol ALOS PALSAR Data	
	Scene 1	Scene 2
Acquisition date	May 16, 2010	April 03, 2011
Wavelength	23.5 cm,	23.5 cm,
	1.27 GHz (L-Band)	1.27 GHz (L-Band)
Spatial resolution	Az: 4.5 m	Az: 4.5 m
	Ra: 9.5 m	Ra: 9.5 m
Level product	P 1.1	P 1.1
Incidence angle at scene center	25.752	23.948
Orbit pass	Ascending	Ascending
Noise equivalent (NE σ^0)	- 30 ~ - 31 dB	- 30 ~ - 31 dB
Absolute geo-location accuracy	< 200 m	< 200 m
Absolute radiometric accuracy	0.7 dB	0.7 dB

In addition, silica sand in the study area almost homogenous type based on the chemical and physical characteristic from the laboratory analysis. The developed model employed with the assumption has the layer which is composed by two layers: the first layer is silica sand and below as the bedrock is the peat layer. The incident wave is assumed as the plane wave with an incident angle (θ_i). The equivalent circuit for the model used in our analysis is shown in Figure 3.6, where the effective impedance of silica sand layer is Z_S , the parallel of peat layer impedance is Z_P , and the total input of impedance is Z_{TS} . To simplify the analysis, the parallel of peat layer impedance (Z_P) is ignored and assumed as zero (perfect conductor). From the method of transmission line theory, the total input impedance Z_{TS} is derived (Figure 3.6) by:

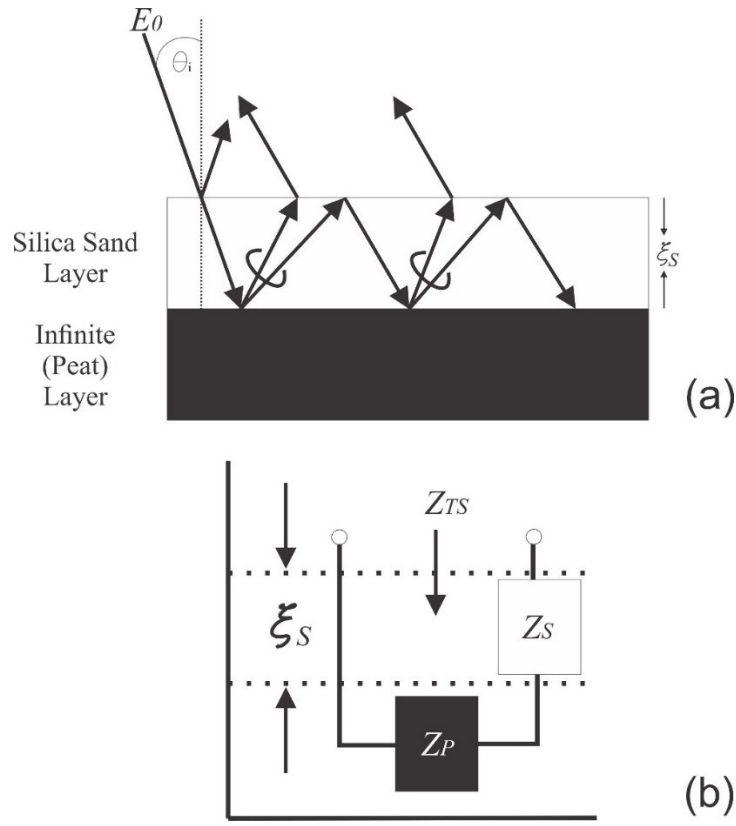


Figure 3.6. (a) Two-dimensional analysis model for composing three layers media; the infinite length of air, the thickness ξ_s of silica sand layer, and infinite depth of Peat layer as the bedrock. (b) The equivalent circuit of the model.

$$Z_{TS} = Z_S \frac{Z_P + Z_S \tanh \gamma_s \xi_s}{Z_S + Z_P \tanh \gamma_s \xi_s} \quad (1)$$

Where γ_s is the constant propagation and ξ_s is the thickness of silica sand layer. Considering the wave transmitted propagation from the air to the surface soil and referring to this study, the constant propagation γ_s is derived from Maxwell's equations as:

$$\gamma_s = j \frac{2\pi}{\lambda_s} \sqrt{\epsilon_{rs} \mu_{rs}} \cos \theta_{ts} \quad (2)$$

Where ϵ_{rs} is the dielectric constant complex, μ_{rs} is the specific permeability complex, θ_{ts} is the transmission angle, and λ_s is wavelength. j is equal to $\sqrt{-1}$.

The impedance wave (Z_s) that comes from the transmitted wave in the silica sand layer is given by the component of the electromagnetic field that perpendicular to the propagation axis.

$$Z_s = E_{yts}/H_{zts} = Z_0 \sqrt{\mu_{rs}/\epsilon_{rs}} \cos \theta_{ts} \quad (3)$$

Where $Z_0(\sqrt{\mu_0/\epsilon_0})$ is the impedance wave in air or free space ($=120 \pi$ ohms).

From Snell's law, the relationship between incidence angle θ_i and transmission angle θ_{ts} , described as:

$$\sin \theta_i / \sin \theta_{ts} = \sqrt{\epsilon_{rs} \mu_{rs}} \quad (4)$$

Substitution to the equation (1) From (2)-(4), the impedance wave Z_{TS} of incident wave in silica sand layer becomes:

$$Z_{TS} = \frac{Z_0}{\epsilon_{rs}} \sqrt{\epsilon_{rs} \mu_{rs} - \sin^2 \theta_i} \tanh \left(j \frac{2\pi \xi_s}{\lambda_s} \sqrt{\epsilon_{rs} \mu_{rs} - \sin^2 \theta_i} \right) \quad (5)$$

From equation (5), the thickness estimation (ξ_s) can be derived as:

$$\begin{aligned} \tanh \left(j \frac{2\pi \xi_s}{\lambda_s} \right) \sqrt{\epsilon_{rs} \mu_{rs} - \sin^2 \theta_i} &= \frac{Z_{TS} \epsilon_{rs}}{Z_0 \sqrt{\epsilon_{rs} \mu_{rs} - \sin^2 \theta_i}} ; \\ e^{2 \left(j \frac{2\pi \xi_s}{\lambda_s} \right) \sqrt{\epsilon_{rs} \mu_{rs} - \sin^2 \theta_i}} - 1 &= \frac{Z_{TS} \epsilon_{rs}}{Z_0 \sqrt{\epsilon_{rs} \mu_{rs} - \sin^2 \theta_i}} \left(e^{2 \left(j \frac{2\pi \xi_s}{\lambda_s} \right) \sqrt{\epsilon_{rs} \mu_{rs} - \sin^2 \theta_i}} + 1 \right) ; \\ \left(j \frac{2\pi \xi_s}{\lambda_s} \right) \sqrt{\epsilon_{rs} \mu_{rs} - \sin^2 \theta_i} &= \frac{1}{2} \ln \left(\frac{1 + \left(\frac{Z_{TS} \epsilon_{rs}}{Z_0 \sqrt{\epsilon_{rs} \mu_{rs} - \sin^2 \theta_i}} \right)}{1 - \left(\frac{Z_{TS} \epsilon_{rs}}{Z_0 \sqrt{\epsilon_{rs} \mu_{rs} - \sin^2 \theta_i}} \right)} \right) ; \end{aligned}$$

$$\xi_S = \frac{\ln \left(\frac{1 + \left(\frac{Z_{TS} \epsilon_{rS}}{Z_0 \sqrt{\epsilon_{rS} \mu_{rS} - \sin^2 \theta_i}} \right)}{1 - \left(\frac{Z_{TS} \epsilon_{rS}}{Z_0 \sqrt{\epsilon_{rS} \mu_{rS} - \sin^2 \theta_i}} \right)} \right)}{4j\pi \sqrt{\epsilon_{rS} \mu_{rS} - \sin^2 \theta_i}}^{\lambda_S} \quad (6)$$

From Fresnel reflectivity coefficient and the total input impedance, the reflection coefficient can be described by substitutes from equation (6) into equation (1).

$$\Gamma^0 = \left| \frac{1 - \sqrt{\epsilon_{rS}}}{1 + \sqrt{\epsilon_{rS}}} \right|^2 \quad (7)$$

$$\Gamma = \Gamma^0 \cos \theta_i \quad (8)$$

Thus, the relationship between reflectivity coefficient and total input impedance Z_{TS} can be described as:

$$\Gamma = \frac{Z_{TS} - Z_0 \cos \theta_i}{Z_{TS} + Z_0 \cos \theta_i} \quad (9)$$

Furthermore, the backscattering coefficient from field $\sigma^0(f)$ is defined as:

$$\sigma_f^0 = 20 \log |\Gamma| \quad (10)$$

Backscattering coefficient $\sigma^0(s)$ (dB) of ALOS PALSAR at a given polarization mode is:

$$\sigma_s^0 = 10 \log_{10}(DN) + CF \quad (11)$$

Where CF is the conversion factor (-83) [30].

From equation (10) and (11) we can get different value of backscattering coefficient from satellite and from the field observations. This differentiation known as average error and defined as:

$$\bar{e} = \overline{\sigma_s^0} - \overline{\sigma_f^0} \quad (12)$$

From differentiation value of backscattering coefficient between satellite and field observations, the ratio also can be detected, and the average ratio can be defined as:

$$\alpha = \frac{\sigma_s^0}{\sigma_f^0}; \quad \bar{\alpha} = \frac{\overline{\sigma_s^0}}{\sigma_f^0} \quad (13)$$

After the differentiation value of backscattering coefficient between satellite and field observations have been detected, the backscattering coefficient correction can be defined as:

$$\sigma_s^0 = \bar{\alpha} \sigma_f^0 \quad (14)$$

The relationship from backscattering coefficient σ^0 and silica sand layer thickness estimation ξ_s can be obtained from equations (5) – (14). Where the dielectric constant complex \mathcal{E}_{rs} of silica sand sample was measured in the laboratory using dielectric probe kit ENA Series Network Analyzer E5062A from frequency range 0.3 to 3.0 GHz.

Scattering decomposition of physical scattering from the incoherent decomposition theorems have been used to show information of this area image, there as, Freeman decomposition [31], [32], [33] and Four-component model [34], [35], [36].

For the scattering mechanisms of Freeman decomposition describes the three physical mechanisms, which are double bounce scattering, surface scattering, and volume scattering:

$$[C] = f_s[C_{surface}] + f_d[C_{double}] + f_v[C_{volume}] \quad (15)$$

According to the model, measurement of power P may be decomposed into three quantities:

$$P_s = f_s(1 + |\beta|^2), \quad P_d = f_d(1 + |\alpha|^2), \quad P_v = \frac{8}{3}f_v, \\ P = P_s + P_d + P_v \quad (16)$$

Four-component scattering which known as Yamaguchi is a model based on Freeman's three-component model, where the covariance matrix $[C]$ or coherency $[T]$ can be denoted as four scattering mechanisms (15, 16):

$$[C] = f_s[C_{surface}] + f_d[C_{double}] + f_v[C_{volume}] + f_c[C_{helix}] \quad (17)$$

Where f_s , f_d , f_v and f_c are the expansion coefficients that needs to be determined. $[C_{surface}]$ and $[C_{double}]$ are identical with those in Freeman decomposition, $[C_{volume}]$ is modified with:

$$10\log(\langle |S_{hh}|^2 \rangle / \langle |S_{vv}|^2 \rangle) \quad (18)$$

And $[C_{helix}]$ was introduced as contribution for encountering the helix scattering power. The scattering powers, P_s , P_d , P_v and P_c are surface, double bounce, volume and helix contributions, respectively, which are obtained as:

$$\begin{aligned} P_s &= f_s(1 + |\beta|^2), & P_d &= f_d(1 + |\alpha|^2), & P_v &= f_v, & P_c &= f_c, \\ P &= P_s + P_d + P_v + P_c \end{aligned} \quad (19)$$

3.2.1 Synthetic Aperture Radar (SAR) scene processing

PALSAR Level 1.1 data has the basic of geocode information, map projection, range compression, single look azimuth compression, complex image data of slant-range, and a single look complex (SLC) that include of the coordinates, phases, and amplitudes.

The physical decomposition was used to process full polarimetry ALOS PALSAR level 1.1 using PolSARpro v5 software. The target decomposition used to provide a dominant scattering mechanism for a pixel or group of pixels. The coherent decomposition is used to show the measured scattering matrix $[S]$ as the combination of scattering response from the simpler object. Distributed scatterers can be characterized using second order polarimetric

representations, which are Covariance [C_3] or Coherence [T_3] matrices. The objective of incoherent decomposition is to separate coherence or covariance as the combination of second order descriptors corresponding to the canonical objects.

PALSAR Geo-referenced images were derived. The images were processed using ASF MapReady 3.1 software. The process (Figure 3.7) of the images were geo-coded with Universal Transverse Mercator (UTM) system and co-registered with 5 main locations which are Beting Aceh (BA) location ($2^{\circ} 6'8.53''N$ and $101^{\circ}34'30.67''E$), Tanjung Api (Tap) location ($2^{\circ} 7'30.46''N$ and $101^{\circ}39'19.92''E$), Teluk Rhu (TRh) location ($2^{\circ} 7'27.61''N$ and $101^{\circ}39'23.65''E$), Tanjung Punai (TPn) location ($2^{\circ} 7'13.91''N$ and $101^{\circ}39'49.61''E$) and Tanjung Lapin (TLp) location ($2^{\circ} 6'47.62''N$ and $101^{\circ}40'36.75''E$) as the ground control points selected manually matched with field observation and also using ENVI 4.8, where the overall error was less than a single pixel with the nearest neighbors resampling was used at this stage. Validation of the images was exported to the .xml file which projected to the Google Earth (Figure 3.8).

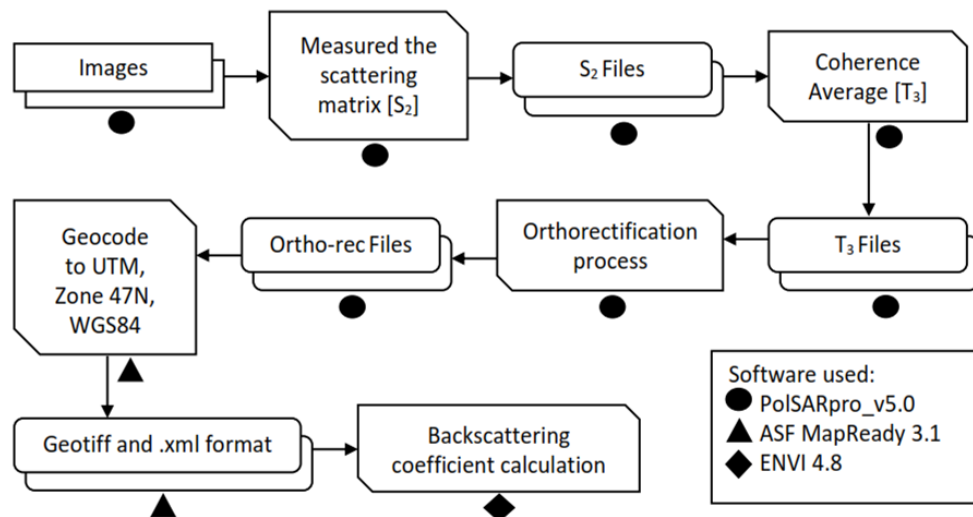


Figure 3.7. Geo-rectification Process of PALSAR Image in This Study.

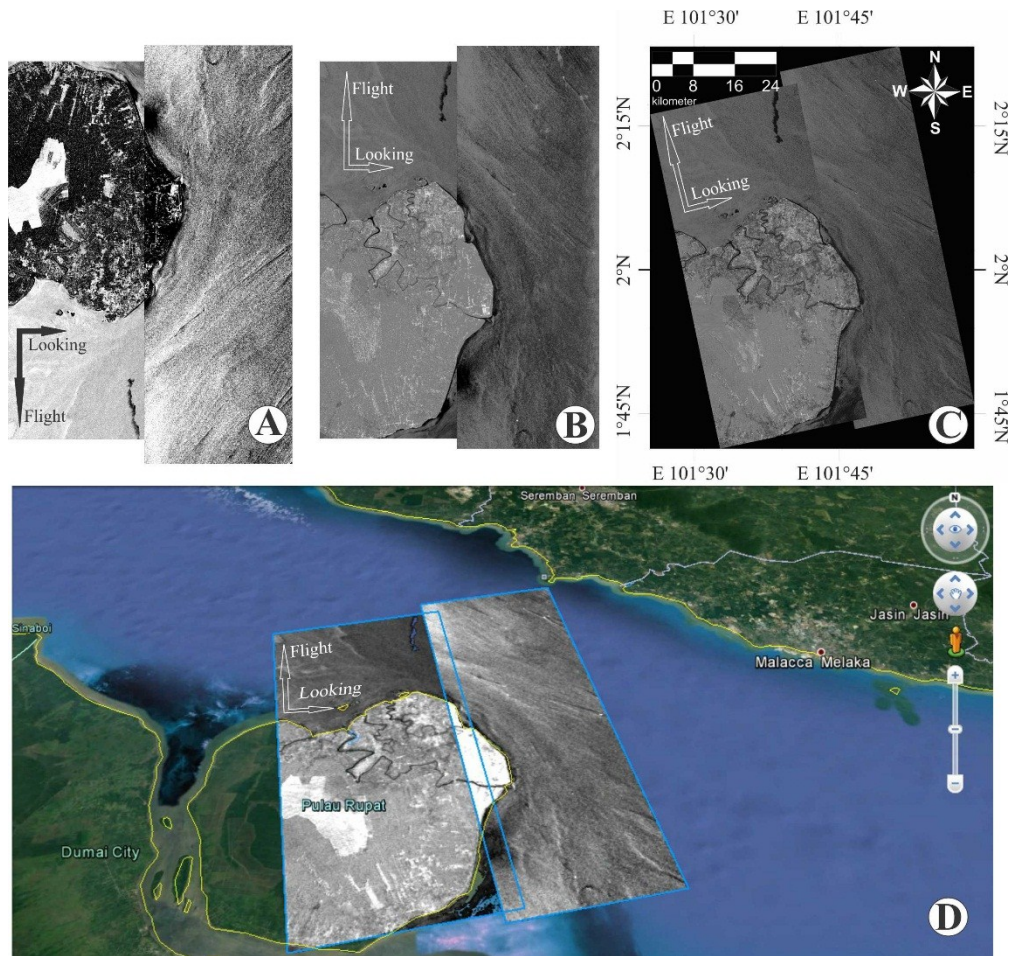


Figure 3.8. The Image Processing Step (a. Before Correction, b. Geometry Correction Process, c. Geo-rectified Image, d. Validation by Projected to the Google Earth).

3.2.1 Sample properties analysis

The dielectric constant is the ratio of the value of capacitor's capacitance on dielectrics with capacitance values in a vacuum condition. The dielectric constant or relative electric permittivity is also defined as a constant that symbolized electrostatic flux meeting in a material when given electric potential. The constant is a comparison of the electrical energy stored in the material if given a potential, relative to a vacuum. Dielectric properties are properties which describe the level of a material's ability to store charge the

electric potential difference is high. In practical terms, the dielectric properties often associated with electrically insulating material placed between two pieces of capacitors.

In this study, the dielectric constant measurement was used as the identity of silica sand sample and its relation to the backscattering coefficient measurement from the SAR data analysis. The step of calculating the dielectric constant as mentioned below (Figure 3.9):

- Turn on the dielectric constant equipment (ENA Series Network Analyzer E5062A) and open the software
- Set the frequency range (L-Band: 1.26-1.275 GHz)
- Set the number point of counting
- Set the water temperature
- Click the calibration (air measurement, probe kit, and water measurement).
- Clean the dielectric constant probe kit
- Put the dielectric constant probe kit into the sample and trigger the measurement

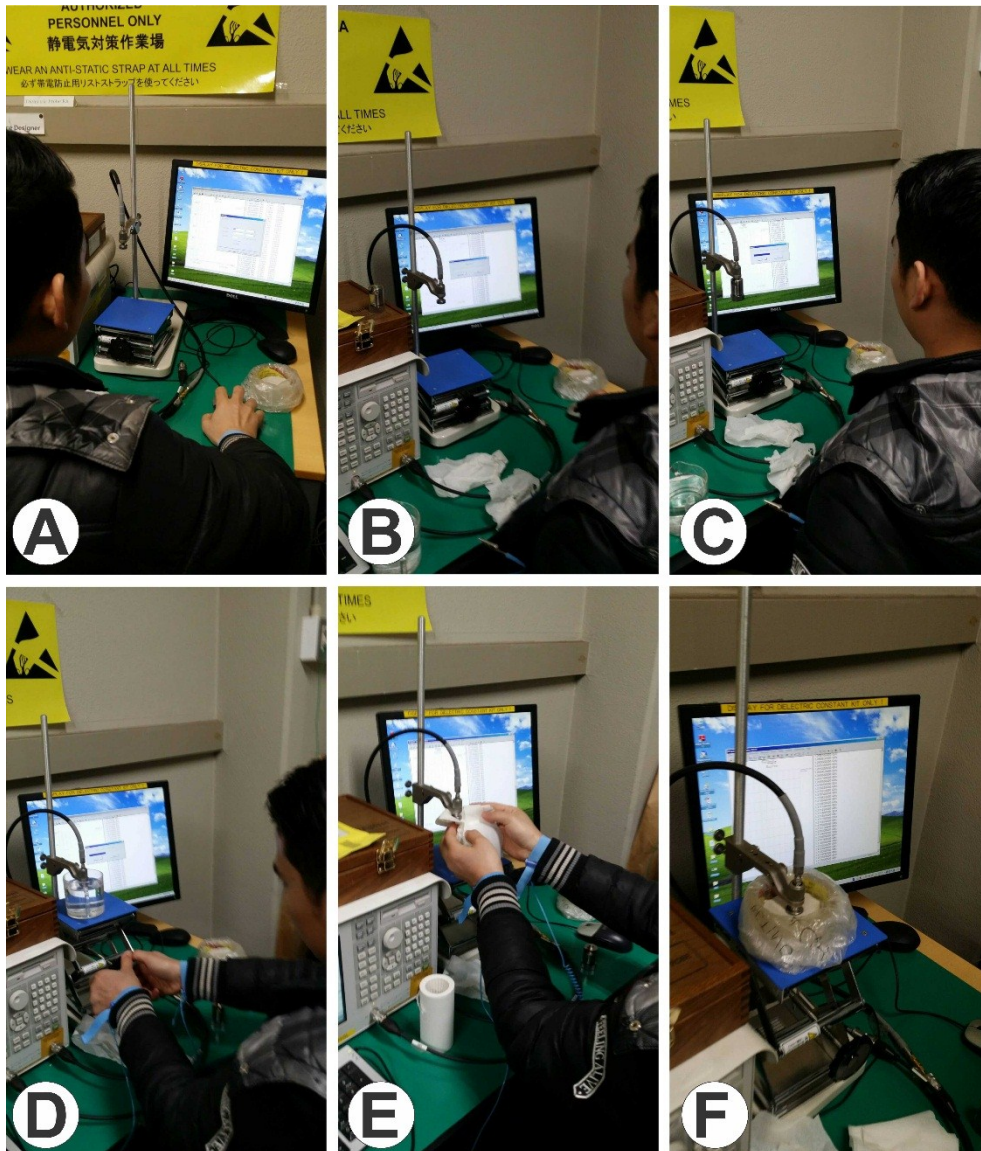


Figure 3.9 The Measurement Process to Calculate Dielectric Constant Value
(A: Setting the parameter; frequency range, and number point of counting,
B-D: Calibration of the air, probe, and water temperature, E: Cleaning the
dielectric probe kit, F: Measuring the sample).

4 RESULT AND DISCUSSION

All samples from the observation location show the properties of sand virtually white and homogeneous by direct observation in the field. It gives the suggestion that the silica sand composition in this region have closely the same silica content. Rock sampling was conducted using geological hammer or other tools. The samples consisted of five main locations which are Beting Aceh (BA), Tanjung Api (TAp), Teluk Rhu (TRh), Tanjung Punai (TPn) and Tanjung Lapin (TLp). The samples from the observation locations show the properties of sand almost white and homogeneous by direct observation in the field [37]. It gives suggestion that the silica sand composition in this region has almost the same silica content for the five main locations which are: Beting Aceh (see Figure 4.1), Tanjung Api (see Figure 4.2), Teluk Rhu (see Figure 4.3), Tanjung Punai (see Figure 4.4) and Tanjung Lapin (see Figure 4.5).



Figure 4.1. The Sample of Silica Sand from Beting Aceh Area.



Figure 4.2. The Sample of Silica Sand from Tanjung Api Area.

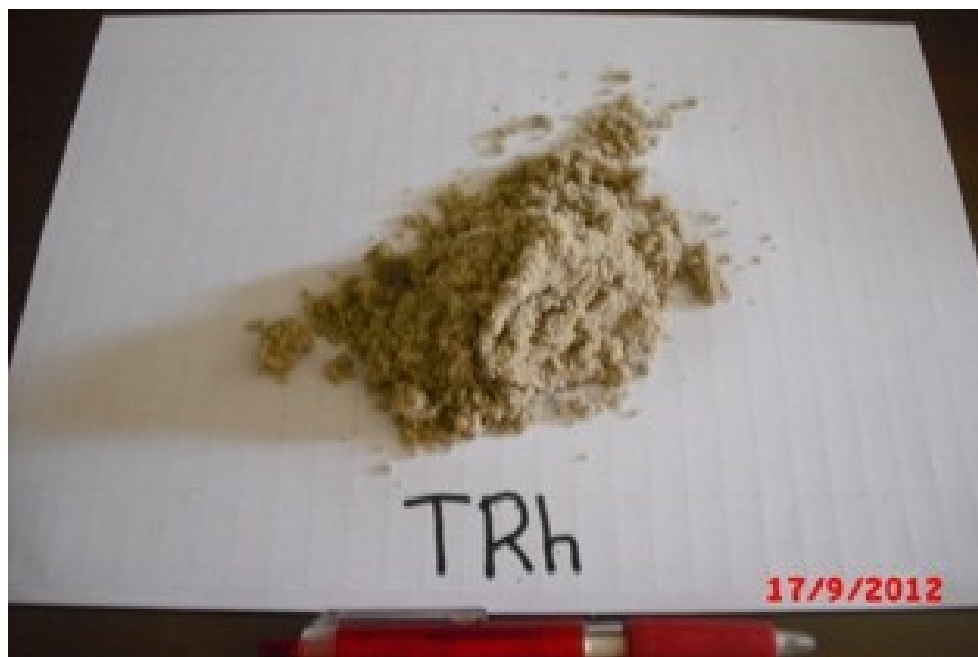


Figure 4.3. The Sample of Silica Sand from Teluk Rhu Area.

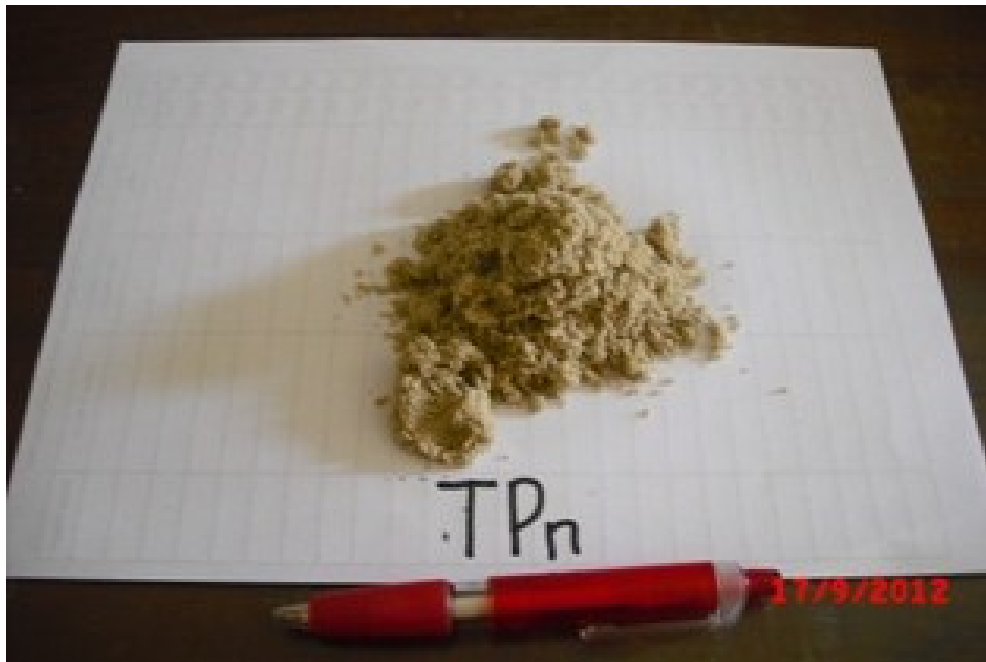


Figure 4.4. The Sample of Silica Sand from Tanjung Punai Area.



Figure 4.5. The Sample of Silica Sand from Tanjung Lapin Area.

4.1 Distribution and the Origin of Silica Sand on the Northern Coastline of Rupert Island

Field observation on the Rupert Island shows the distribution of silica sand in this island is not located along the entire coastline of the island (Figure 4.6). Silica sand can be found only in the northern part of the coastline, start from Tanjung Mumbul until Pasir Putih area (see Figure 2.3).

Distribution of silica sand in this island is heavily influenced by the current of Malacca Strait as the sediment transport agent (Figure 4.7). The northern part of the island Rupert is dealing directly with the Malacca Strait. Malacca Strait is located between Malaysia Peninsular and Sumatra Island. This strait is the one of meeting point between the Indian Ocean in the northwest and the South China Sea in the northeast and brought the sediment source as the transport agent from both of those seas.

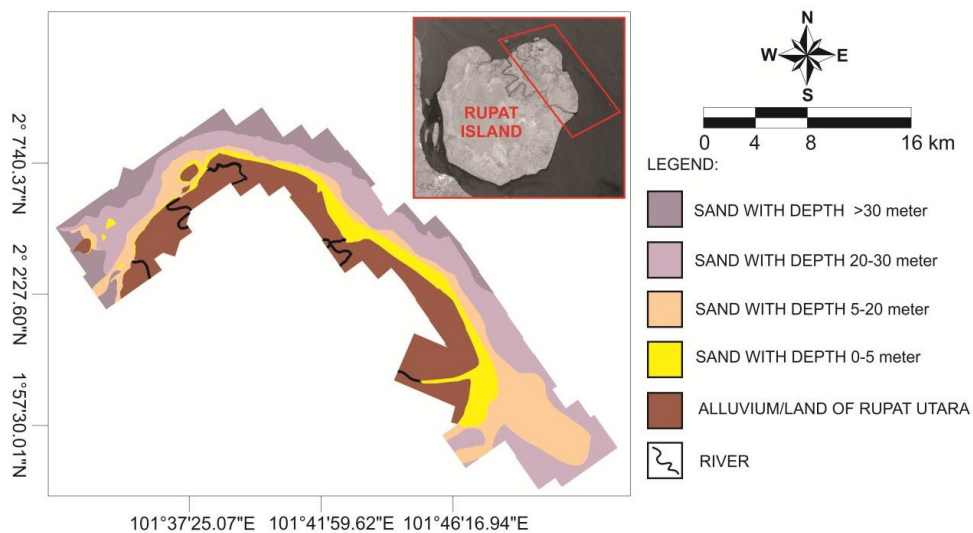


Figure 4.6. The Estimation of Silica Sand Distribution from the field observation.

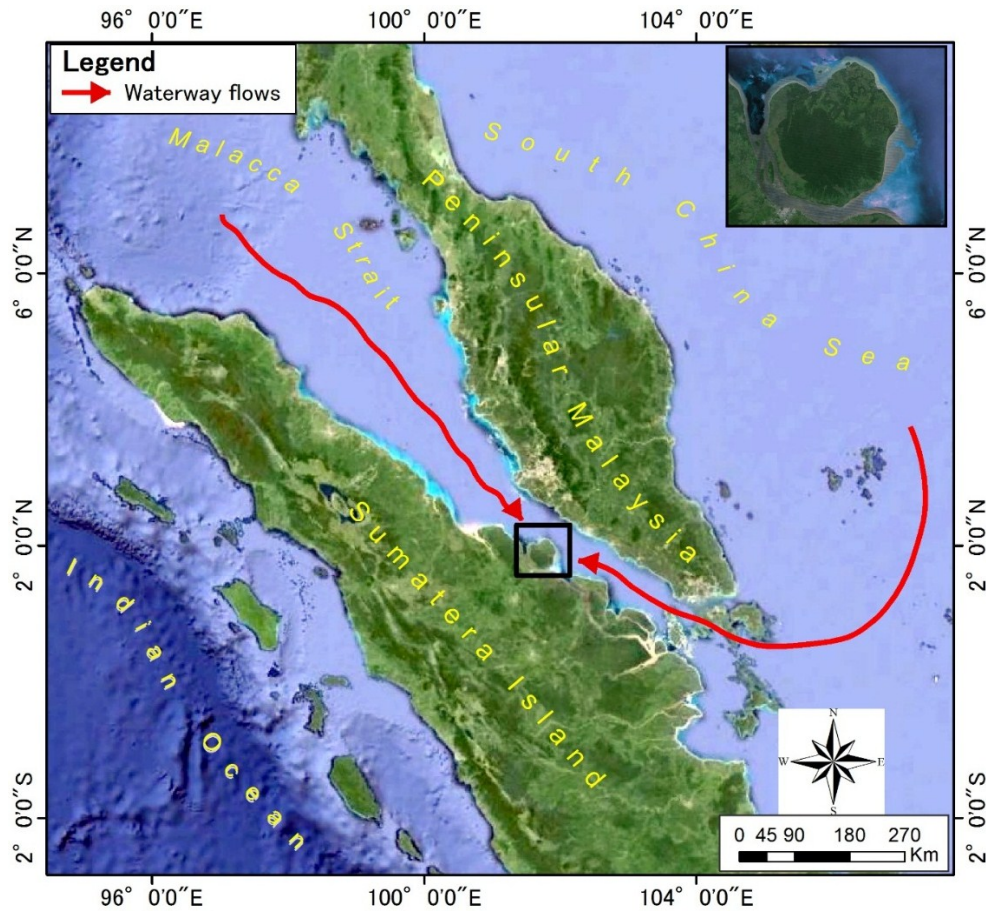


Figure 4.7. Waterway Flows of Malacca Strait as a Sediment Transport Agent for the Silica Sand Sedimentation.

Silica sand presence on the Rupert Island could not be separated from the role held by the Malacca Strait. Silica sand was brought from the current of both seas above at Malacca Strait. The source rocks are composed of igneous rocks, which had been abundant with quartz / silica mineral, especially the South China Sea through the Riau Islands province (which is known as the very rich igneous rock's area) before entering the Malacca Strait.

The origin of Silica sand on Rupert Island is not from the bedrock of this island. The northern island which facing the Malacca Strait gains sand sediment supply from the waterway flows. Malacca Strait transports the sand sediment material from the Indian Ocean at northwestern, while in the north-

eastern, sand sediment materials was obtained from the South China Sea and Riau Islands (see Figure 4.7). There are many sources of sand on the northern part of this island. This is because the current that carried the sediment source was blocked on the northern part of the Rupert Island and deposited the sand on the northern coast of the island. The silica sand comes from Malacca Strait as the transportation agent of sediment. Compared to the bedrock of Rupert Island, which consists of Recent Surface Sediment (Qh) and Older Surface Sediment (Qp), which are consisted of clay and peat as the general composition, it is impossible for these bedrocks to produce sand grain.

Apart from the bedrock of Rupert Island is unlikely to produce silica sand, the origin of silica sand source also proved by the result of the microscopic photograph that shows the grain shape of silica sand particles is rounded. It suggests the source/origin of silica sand came from the far location. The microscopic photograph five main locations (Beting Aceh (see Figure 4.8), Tanjung Api (see Figure 4.9), Teluk Rhu (see Figure 4.10), Tanjung Punai (see Figure 4.11) and Tanjung Lapin (see Figure 4.12)) represents the study area in Beting Aceh, Tanjung Api, Teluk Rhu, Tanjung Punai, and Tanjung Lapin. The microscopic photograph to show the grain size of silica grain was taken, the grain size of silica sand particles that have virtually the identical size and shape.

Refer to the sedimentary provenance and its associations with sedimentary transportation agent [38], [39], sedimentary grain shape and grain size characteristic of silica sand on the northern coastline of Rupert Island are rounded and the shape size is virtually identical. This mean silica sand was transported from far location / source. This analysis also supported that silica sand was not produced by this island bedrock.

All samples from the observation locations shown the properties of silica sand are virtually white and homogeneous by direct observation in the field. It

gives the suggestion that silica sand composition in this area almost have the same content (Figure 4.13).

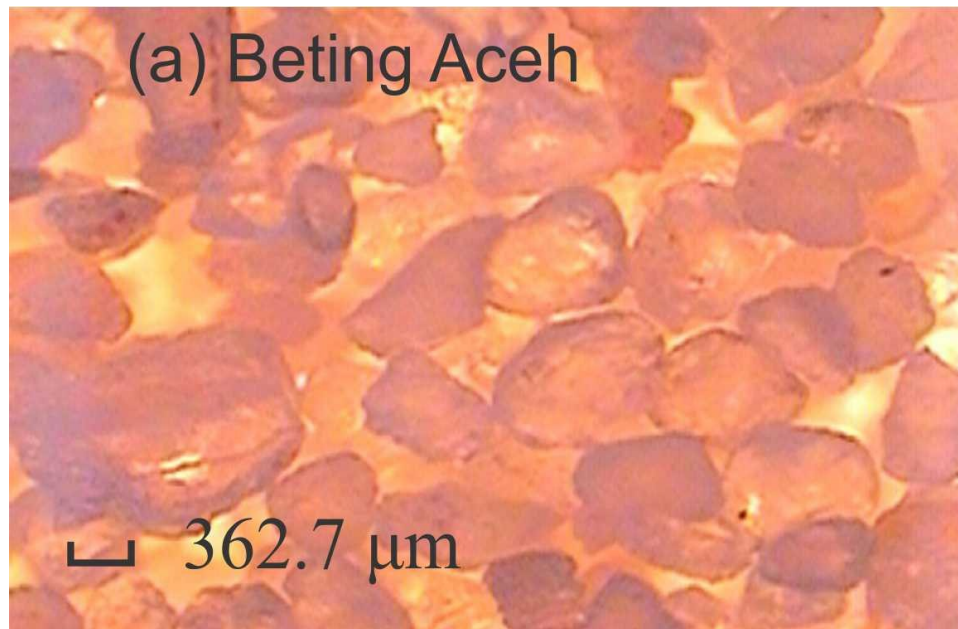


Figure 4.8. Grain Size from Microscopic Photograph of Silica Sand Samples from Beting Aceh Location.

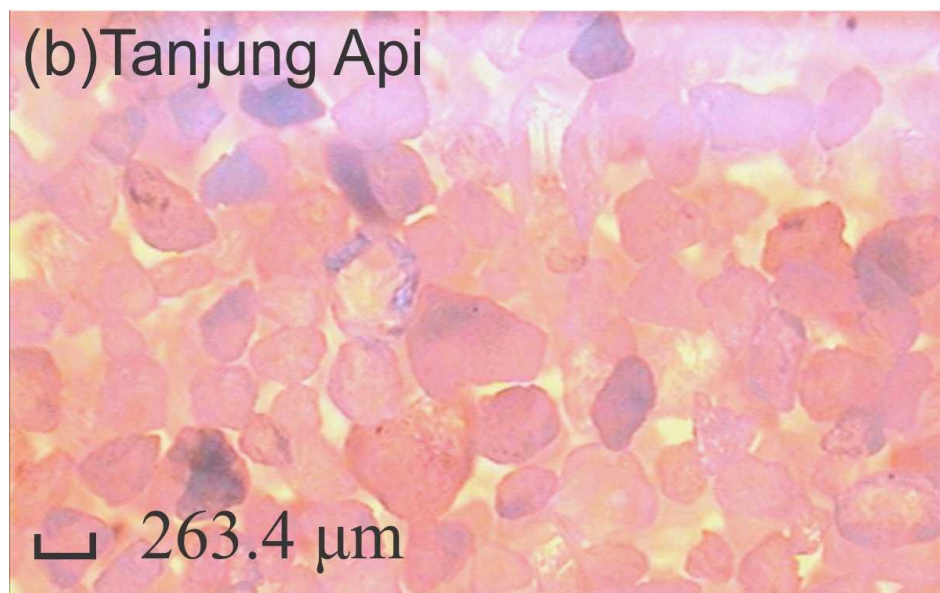


Figure 4.9. Grain Size from Microscopic Photograph of Silica Sand Samples from Tanjung Api Location.

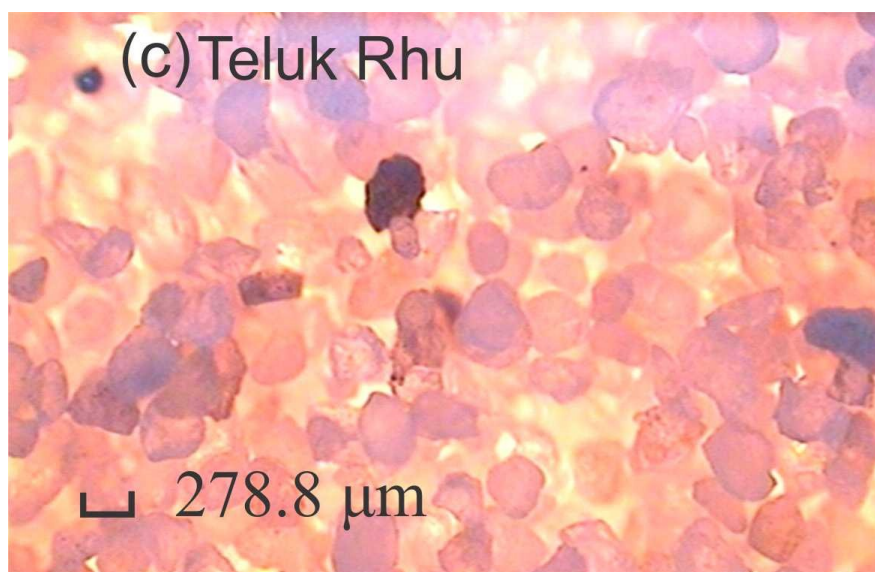


Figure 4.10. Grain Size from Microscopic Photograph of Silica Sand Samples from Teluk Rhu Location.

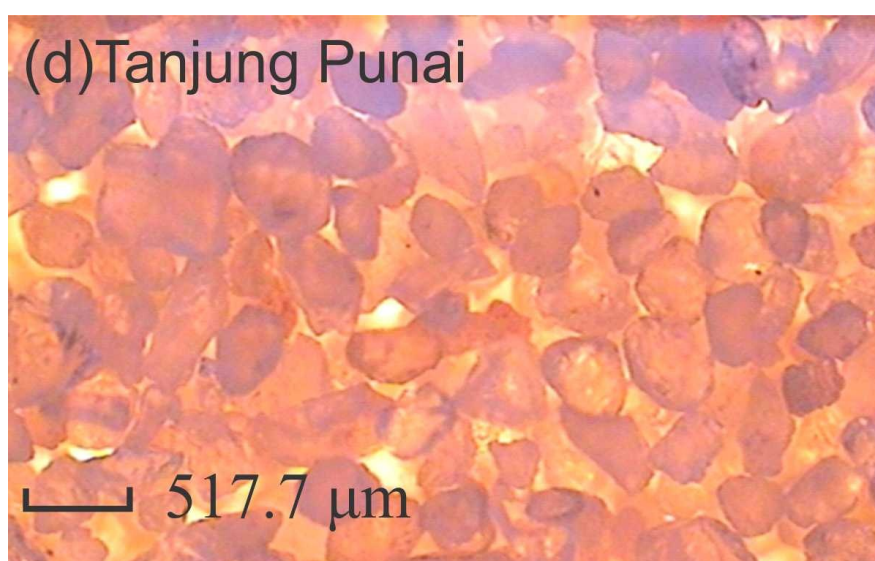


Figure 4.11. Grain Size from Microscopic Photograph of Silica Sand Samples from Tanjung Punai Location.

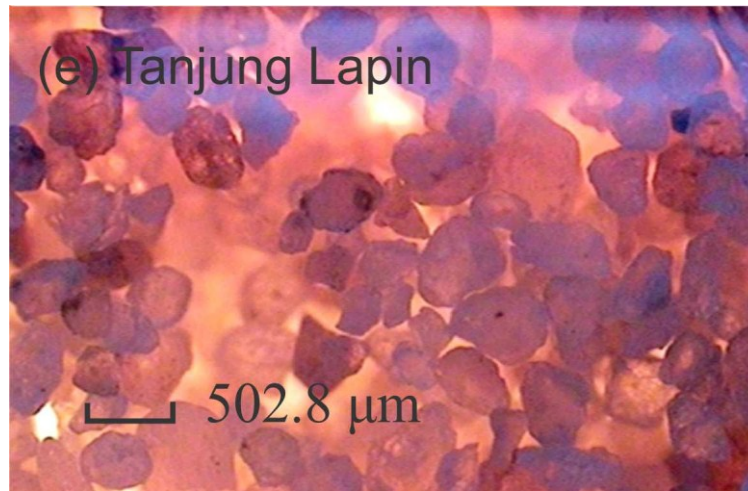


Figure 4.12. Grain Size from Microscopic Photograph of Silica Sand Samples from Tanjung Lapin Location.

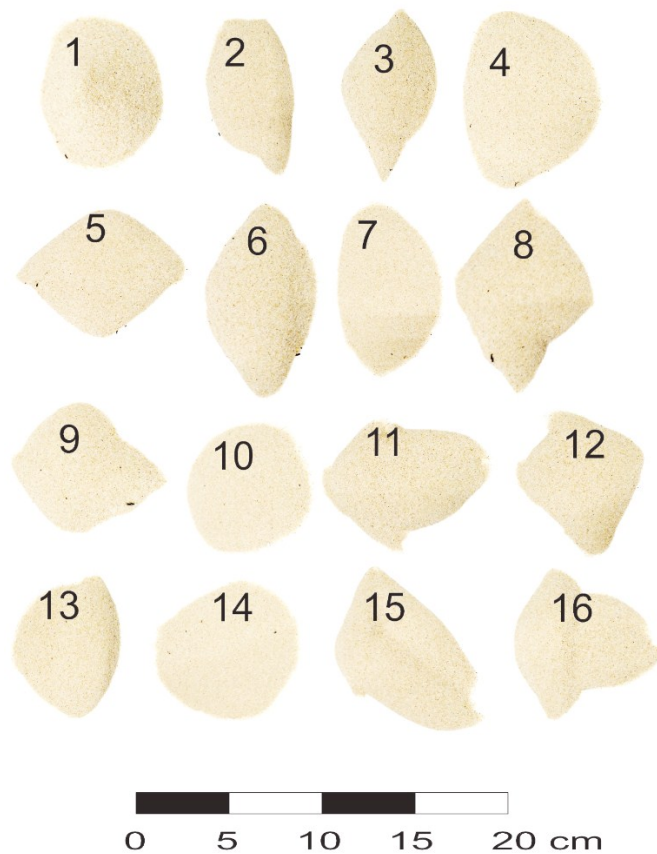


Figure 4.13. Silica Sand Samples from the Northern Coastline of Rupat Island.

4.2 The Percentage of Silica Compound

Determination of the compound of silica percentage and the compound of mineral properties, laboratory testing was used in the sand samples obtained from the field survey. The chemical analysis of silica sand samples needs to get the types of compounds/elements, physical properties and percentage content of the compounds/elements.

Laboratory test using XRF (X-Ray Fluorescence) shows the abundance of compounds: SiO_2 (Silicon dioxide), TiO_2 (Titanium dioxide), Al_2O_3 (Aluminum oxide), Fe_2O_3 (ferric oxide), MnO (Manganese (II) oxide), MgO (Magnesium oxide), CaO (Calcium oxide), Na_2O (Sodium oxide), K_2O (Potassium oxide) and P_2O_5 (diphosphorus pentoxide). The result shows the compound of silica (SiO_2) has the high percentage amount above 95% compare to the other minerals in the same samples. The second abundances mineral in these samples is Al_2O_3 , which the average number of it percentages around 0.70% and followed by another mineral as the small number of the samples from northern part of Rupert Island. XRF test shows the percentage content of compounds/minerals (Table 4.1) for five observation locations (Beting Aceh, Tanjung Api, Teluk Rhu, Tanjung Punai and Tanjung Lapin).

From laboratory test using XRD (X-Ray Diffraction) instrumentation, the result show of quartz mineral abundance. It summarizes the content of quartz mineral fully-loaded in those samples. The samples were measured based on the in-situ sample of the silica sand on the northern coastline of Rupert Island. XRD results show other minerals in the sample, but the total is very small compared to the quartz mineral. The result showed that quartz mineral is a dominant mineral in the samples and can be concluded as the homogeneous quartz sand samples. By this conclusion, the samples taken from this area can be defined as the homogeneous quartz sand which is distributed along the northern part of the Rupert Island area.

Table 4.1. X-RF Result of Silica Percentages of the Silica Sand Samples from Northern Part of Rupert Island.

Compound/ Mineral	Percentage (%)				
	Beting Aceh (BA)	Tanjung Api (TAp)	Teluk Rhu (TRh)	Tanjung Punai (TPn)	Tanjung Lapin (TLp)
SiO ₂	98.42	97.89	97.45	97.83	98.06
TiO ₂	0.19	0.09	0.09	0.07	0.26
Al ₂ O ₃	0.55	0.69	0.85	0.67	0.65
Fe ₂ O ₃	0.38	0.35	0.36	0.36	0.48
MnO	bdl*	bdl*	bdl*	bdl*	bdl*
MgO	0.10	0.10	0.10	0.12	0.12
CaO	0.18	0.20	0.21	0.20	0.20
Na ₂ O	0.05	0.65	0.19	0.09	0.07
K ₂ O	0.22	0.32	0.48	0.32	0.23
P ₂ O ₅	0.01	0.01	0.01	0.01	0.01
L.O.I**	0.40	0.32	0.33	0.41	0.41

*bdl: below detection limit

**L.O.I: lost on ignition

From Figure 4.14, the highest peak of the XRD result shows the quartz mineral is on 1650 in CPS (count per second). From Figure 4.15, the highest peak of quartz mineral (silica mineral) is on the 1800 CPS. Continue to the Figure 4.16, the highest peak of the quartz mineral is on the 1850 CPS. From Figure 4.17, shows the highest peak of quartz mineral is on the 1600 CPS. The last result taken from XRD testing, Figure 4.18, shows the highest peak of quartz mineral is on the 2100 CPS. The highest peak shows the dominant mineral in the sample, while the other peak shows the abundance of mineral.

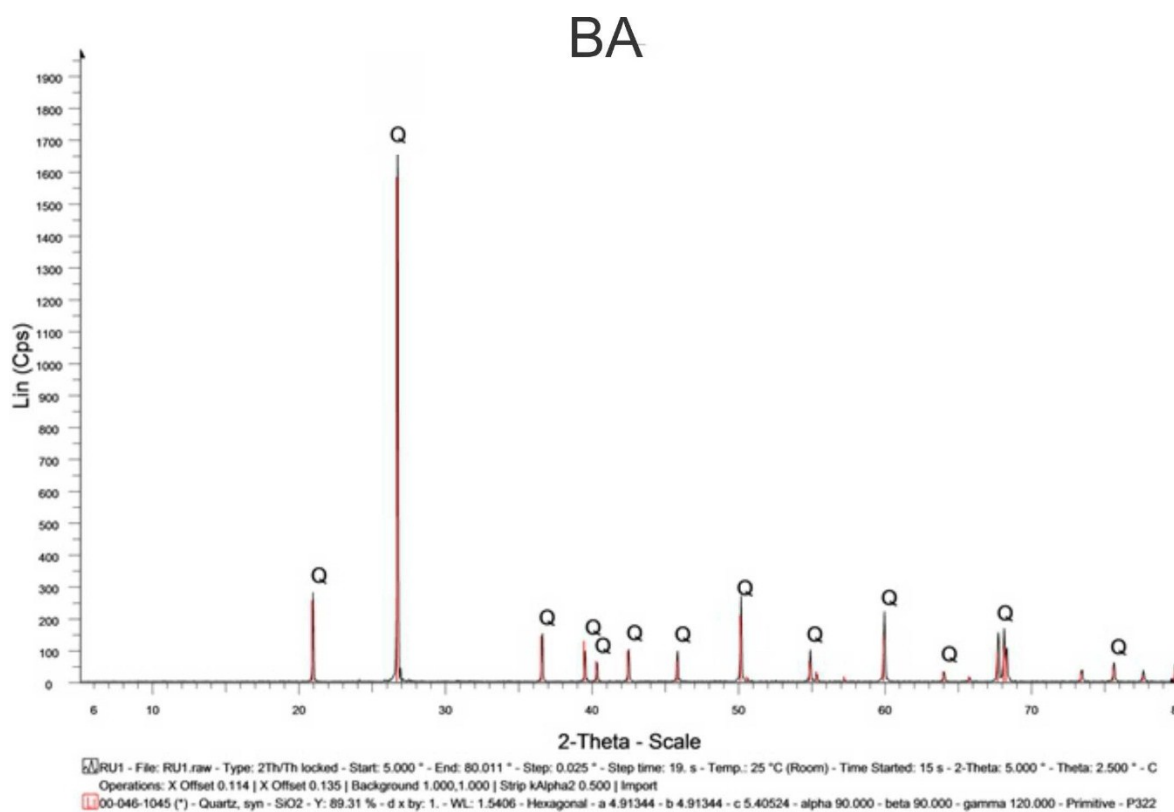


Figure 4.14. The Profile of X-Ray Diffraction from Beting Aceh (BA) Sample.

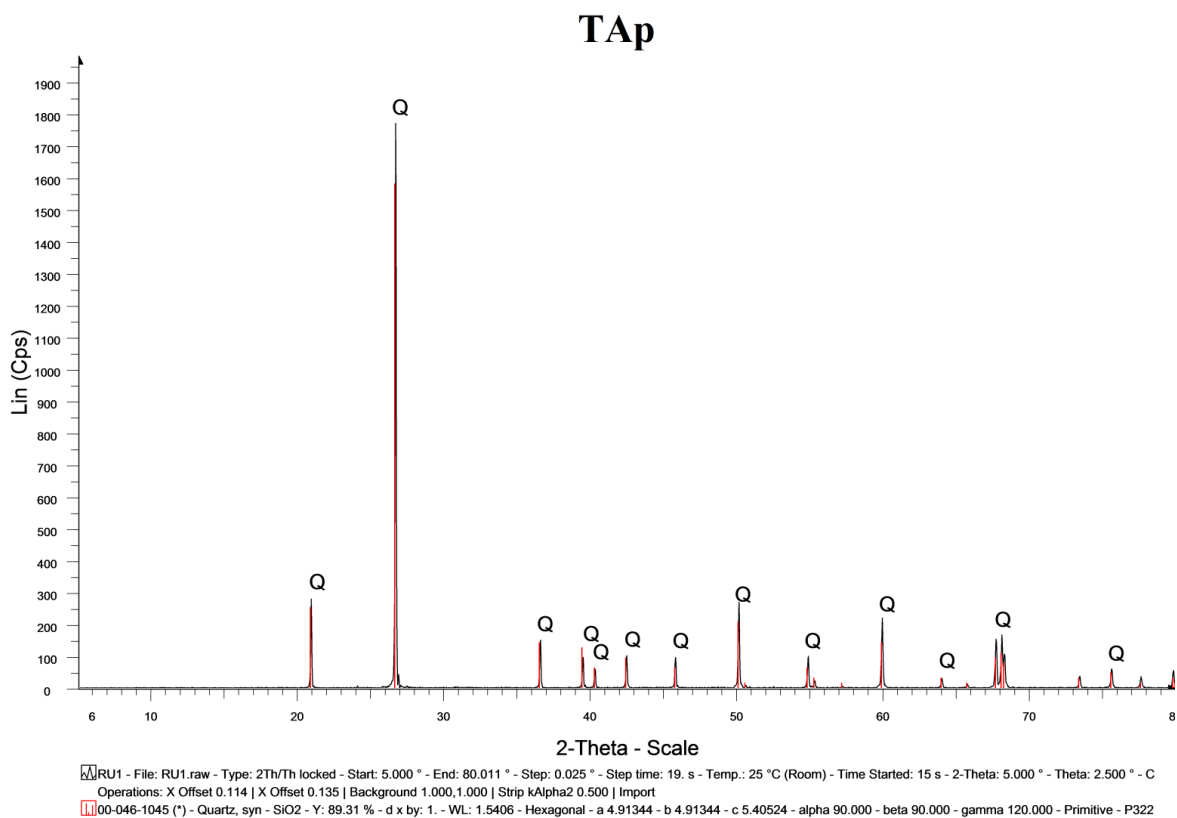


Figure 4.15. The Profile of X-Ray Diffraction from Tanjung Api (TAp) Sample.

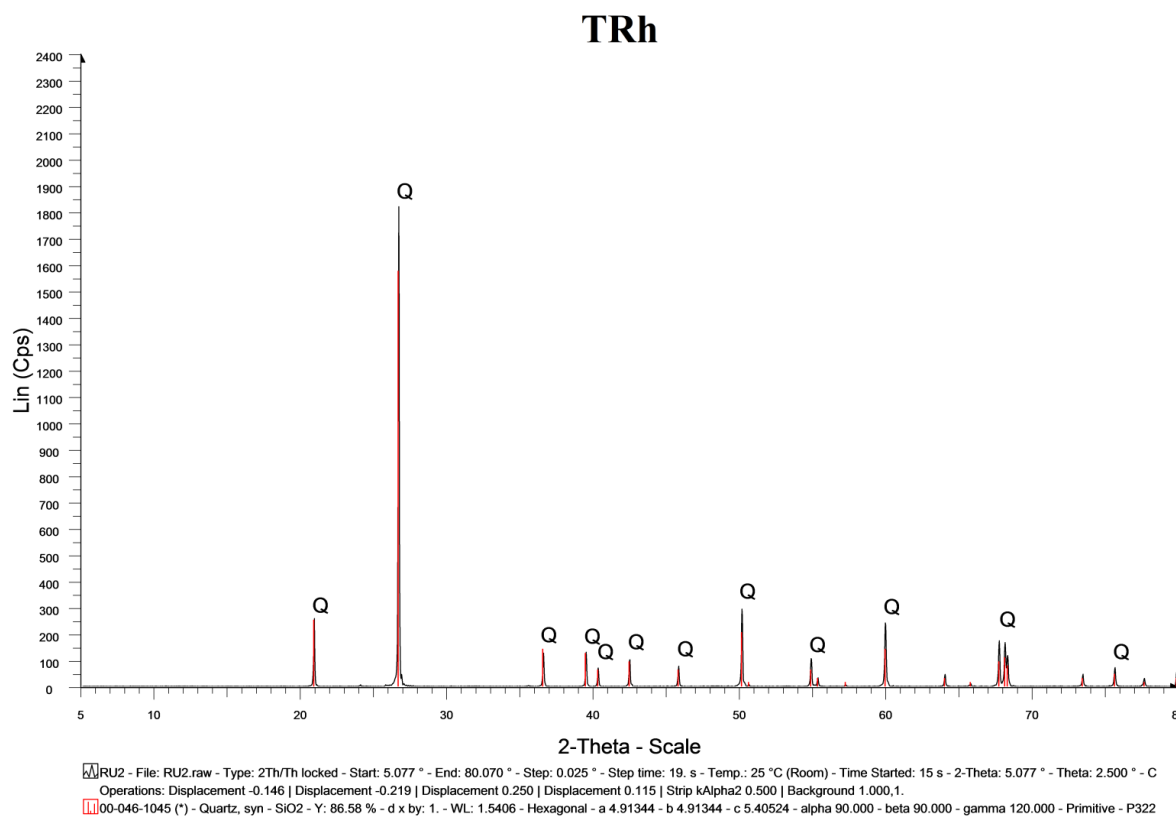


Figure 4.16. The Profile of X-Ray Diffraction from Teluk Rhu (TRh) Sample.

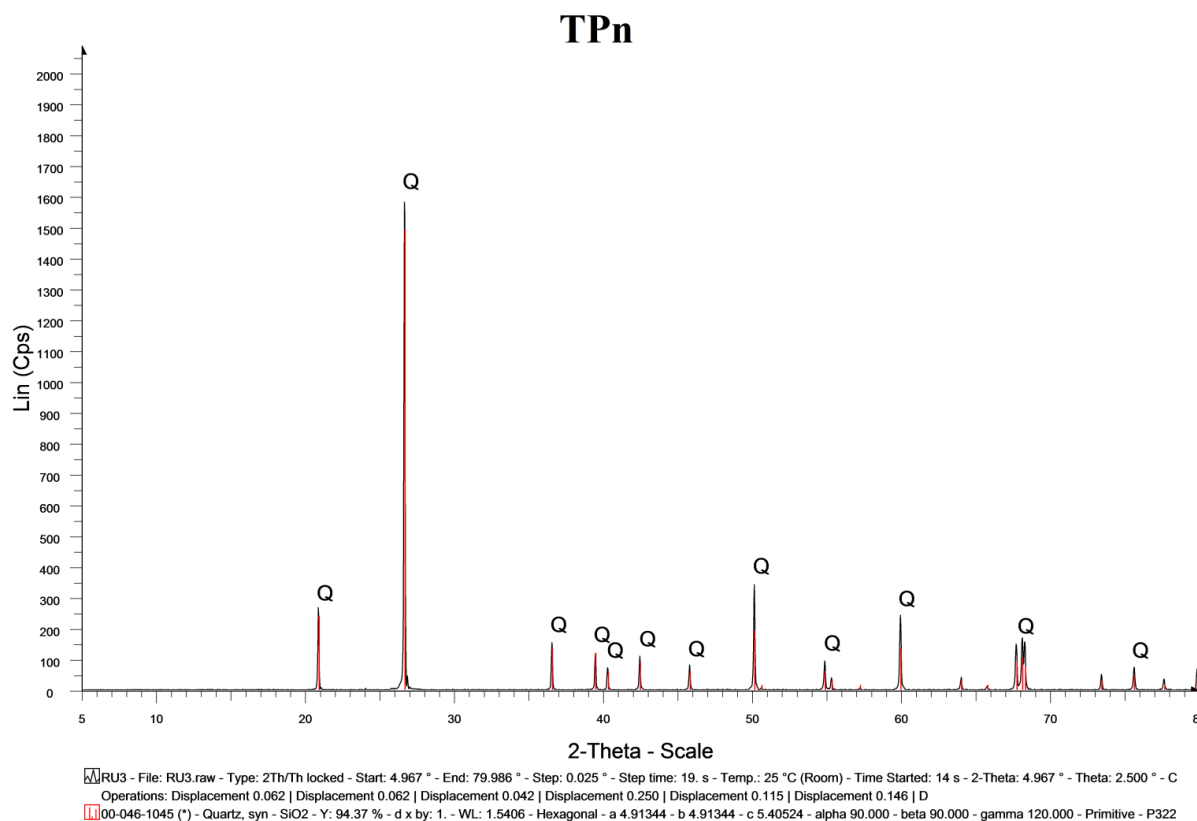


Figure 4.17. The Profile of X-Ray Diffraction from Tanjung Punai (TPn) Sample.

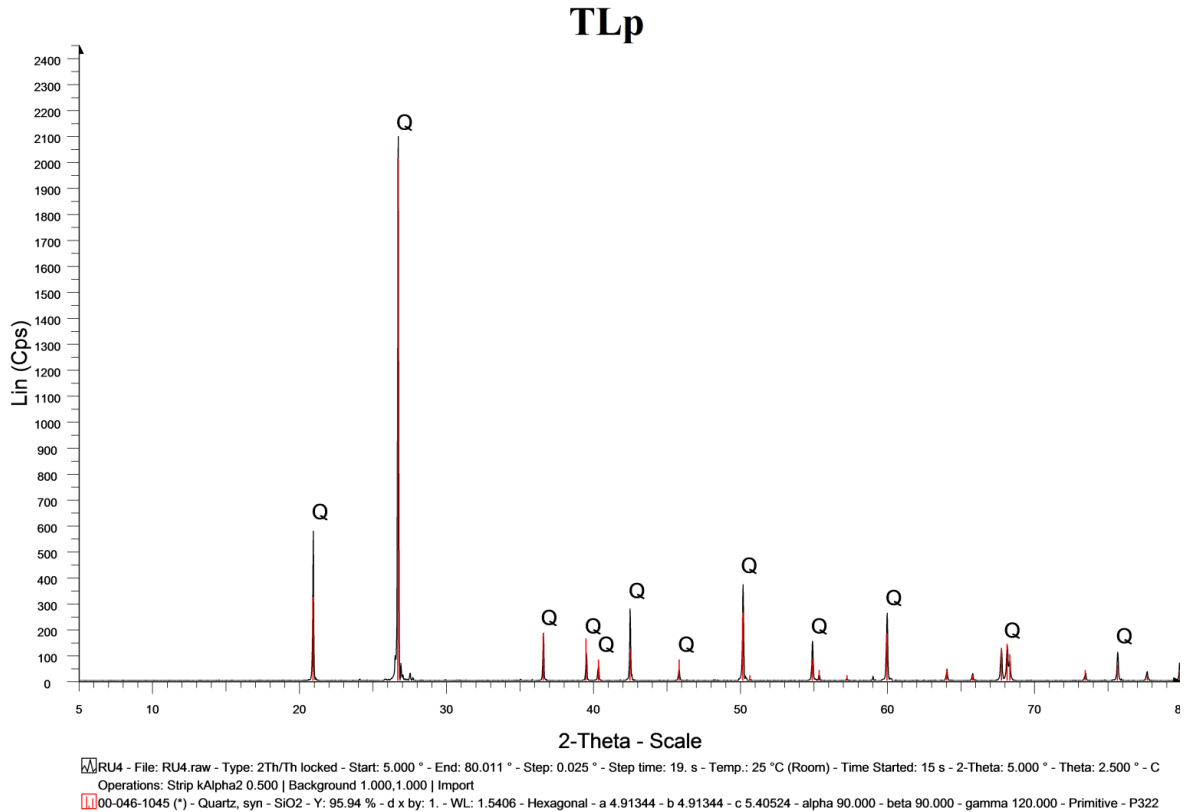


Figure 4.18. The Profile of X-Ray Diffraction from Tanjung Lapin (TLp) Sample.

4.3 Result of Synthetic Aperture Radar (SAR) Data and Sample Analysis

Two adjacent scenes of ALOS PALSAR full-polarimetry data have been used for this study (refer to Table 3.1). From the equation (9) – (13) the differentiation value of backscattering coefficient between satellite and field observations has been calculated (Table 4.2). This differentiation is an error caused by the object orientation while measured from those. The error of object measurement using field observation and satellite methods caused by surface roughness, multiple scatterings, multiple objects at the same area (which mean has multiple dielectrics constant), water content, humidity, weather condition, differentiation of incidence angle between field and

satellite image measurement. From these conditions, the average error can be defined after measuring the samples taken from the field.

Table 4.2. Table of backscattering coefficient Value from ALOS PALSAR and field, average error and average ratio.

Location	Dielectric constant	Backscattering coefficient of field	Backscattering coefficient of ALOS PALSAR	Ratio
1	2.972	-53	-59	1.11
2	2.359	-49	-52	1.06
3	2.259	-50	-54	1.08
4	2.359	-49	-51	1.04
5	2.159	-51	-56	1.1
6	2.259	-50	-53	1.06
7	2.891	-56	-58	1.06
8	2.362	-42	-50	1.19
9	2.892	-54	-55	1.02
10	2.972	-53	-57	1.08
11	2.421	-48	-53	1.04
12	2.359	-49	-53	1.08
13	2.821	-55	-58	1.05
14	2.259	-50	-52	1.04
15	2.891	-56	-57	1.02
16	2.259	-50	-55	1.1
Average		-50.94	-54.56	1.07

The total average error (\bar{e}) is: $(-54.56) - (-50.94) = -3.62$

The total average ratio ($\bar{\alpha}$) is = 1.07

The relationship graphs between backscattering coefficient from satellite and field observations shown in Figure 4.19. Based on the sample properties measurement, dielectric constant shown an important factor influenced the value of backscattering coefficient compared with the other factors.

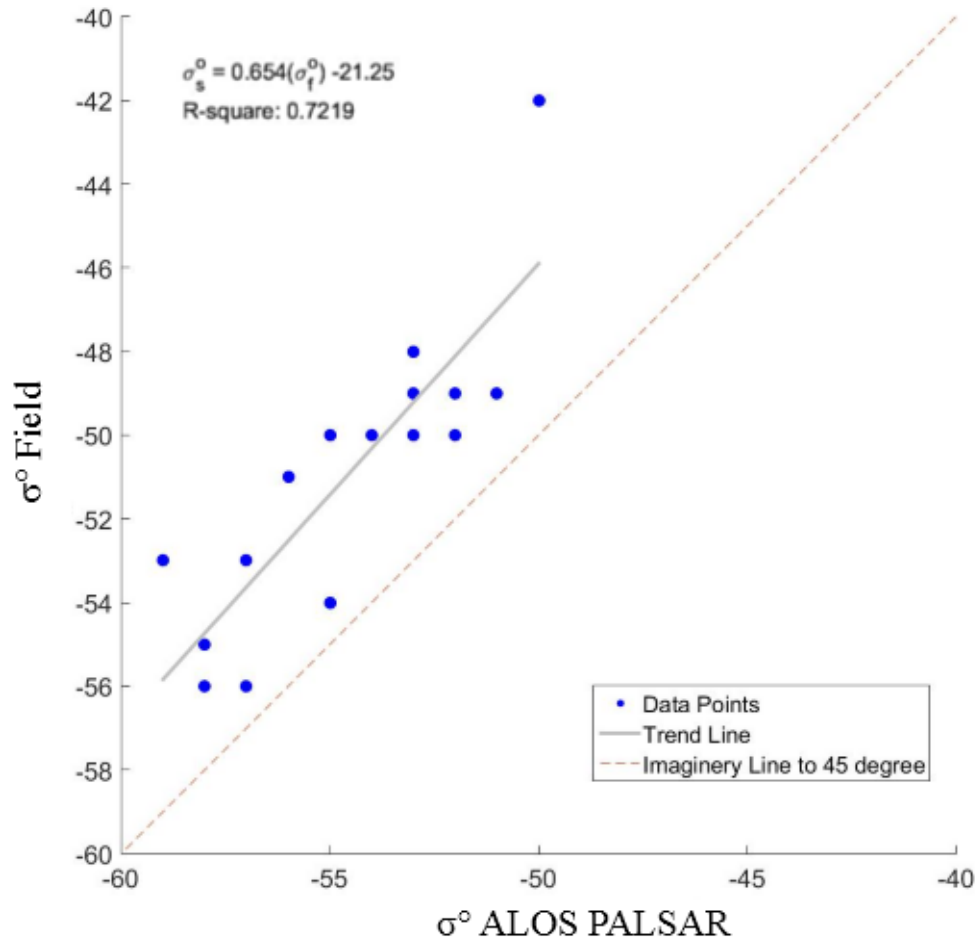
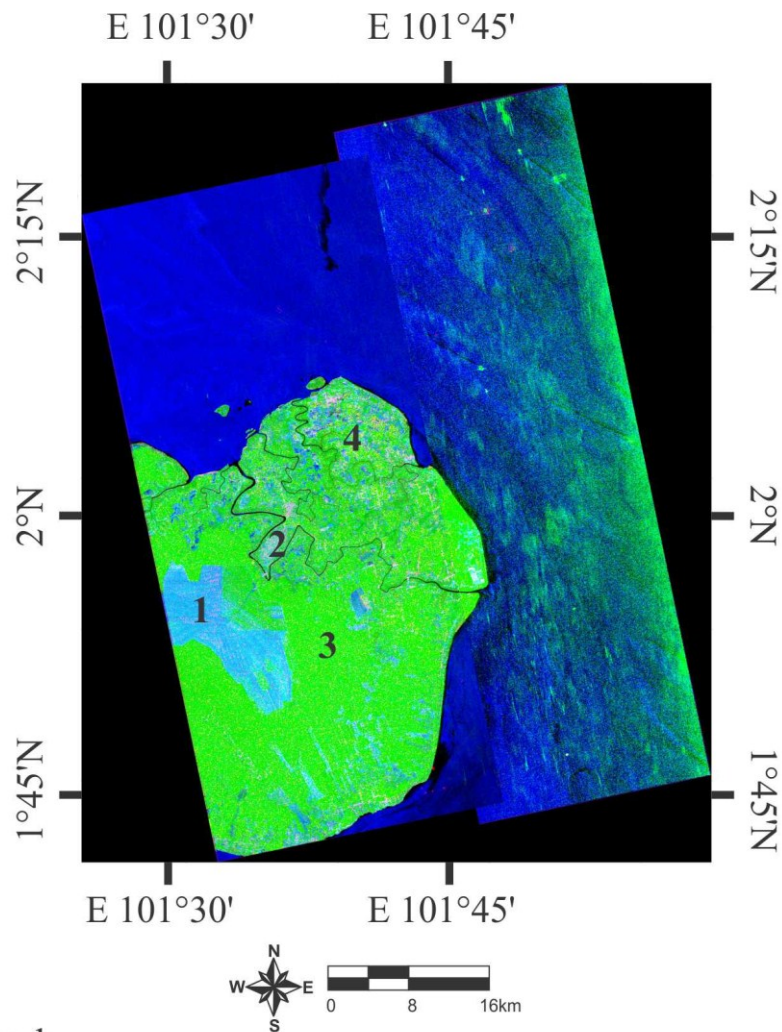


Figure 4.19. The relationship graph between backscattering coefficient from satellite and field observations.

Freeman-Durdeen (Figure 4.20) and Yamaguchi (Figure 4.21) techniques have been used to get the scattering decomposition of physical scattering from the object model based on the incoherent. These techniques are based on the physical scattering which used 3 physical scattering types (Freeman-Durdeen) which are Volume scattering, Double bounce scattering, Surface scattering, and, and for 4 physical scattering types: Surface scattering, Volume scattering, Double bounce scattering, and Helix scattering have been used from Yamaguchi technique. These techniques were used to show the image of Rupert Island by using two adjacent images of ALOS PALSAR. In

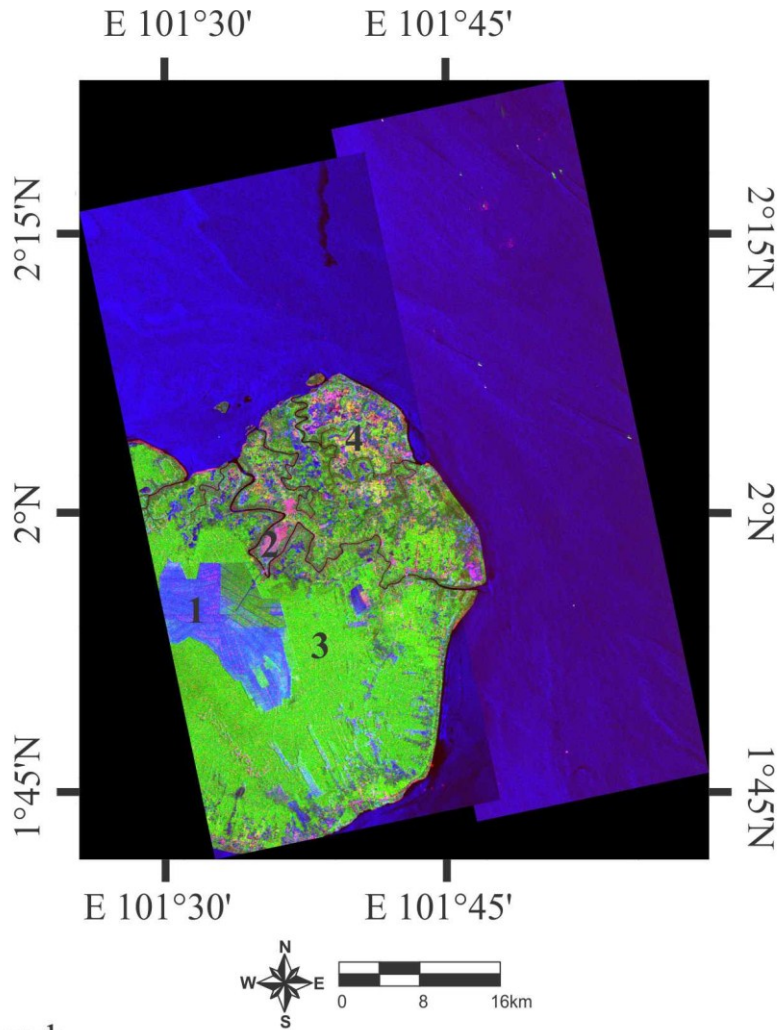
this study area, double bounce scattering represents in red to pink color, surface scattering is blue color in its representative, volume scattering is green color and helix scattering is yellow color. Silica sand distribution has dark color in their representation. This dark colour given by the surface roughness of silica sand distribution is almost flat (see Figure 4.22).



Legend:

- | | |
|-----------------------------------|------------------------------|
| 1: Farmland (oil palm plantation) | 3: Forest/Canopy area |
| 2: Forest area | 4: Complex area (urban area) |

Figure 4.20. Freeman-Durdeen Decomposition from Two Adjacent Scenes of Rupert Island.



Legend:

- | | |
|-----------------------------------|------------------------------|
| 1: Farmland (oil palm plantation) | 3: Forest/Canopy area |
| 2: Forest area | 4: Complex area (urban area) |

Figure 4.21. Yamaguchi Decomposition from Two Adjacent Scenes of Rupert Island.

The model of scattering is based on the covariance matrix (three-component) was successfully applied to decompose Polarimetric SAR's image by the reflection symmetry condition $\langle S_{hh}S_{hv}^* \rangle \approx \langle S_{vv}S_{hv}^* \rangle \approx 0$. This method caused by the simplify of physical scattering mechanisms (volume scattering, surface scattering, and double bounce scattering), which are shown in Figure 4.20 and Figure 4.21, the contributions of each scattering mechanisms to the total

power are shown for each pixel. The blue colour is for Surface scattering, the green colour is for volume scattering, and the red colour is for double bounce scattering. The result from Figure 4.20 and Figure 4.21 show the volume scattering is the best for forest area. The surface scattering and double-bounce scattering are the dominant for farmland. It can be interpreted as the indication that the longer wavelengths can penetrate the relatively short vegetation in plantation area, and the backscatter is mostly from the underlying ground. Therefore, Freeman decomposition can show very well for the different natural targets and very powerful for Polarimetric SAR decomposition for natural distributed object target interpretation. However, the buildings, forest and man-made are also present in the volume scattering, thus this model cannot distinguish from those.

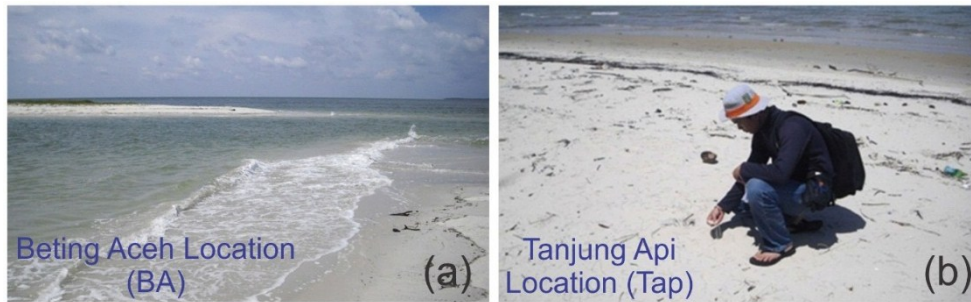


Figure 4.22. Flat condition from the Distribution of silica sand on the northern coastline of Rupert Island, (a) Beting Aceh Location, (b) Tanjung Api Location.

Compared with Freeman-Durden model, the power of helix scattering, corresponding to $\langle S_{hh}S_{hv}^* \rangle \neq 0$ and $\langle S_{vv}S_{hv}^* \rangle \neq 0$, is introduced for more general scattering mechanism as the fourth component by Yamaguchi, which often appears in area of complex urban whereas disappears in almost target of all natural object. This term is essentially caused by the helix scattering matrix and is relevant for the building or human-made structures which has complicated shapes (predominant in urban areas). Furthermore, the change of the probability of the density function for the associated orientation angles

has been modified for the volume scattering component for vegetation, and the choice between the symmetric and the asymmetric covariance can be determined by $10\log(\langle |S_{hh}|^2 \rangle / \langle |S_{vv}|^2 \rangle)$ of the image.

The decomposed result of the covariance matrix with Ps (blue), Pd (red), and Pv (green) is shown in Figure 4.20 and Figure 4.21, the strongest scattering in the forest area is Pv (green). Most farmland in blue indicates that there is no other scattering mechanism except single bounce scattering. Pink colour indicates that both surface scattering and double-bounce scattering exist in some farmland. Overall, the decomposition result is acceptable.

In the urban area, when the flight path is not parallel to the orientation of building blocks, is skew-oriented buildings produce a rather predominant HV component. Therefore, the helix scattering component Pc appears strong in these areas as shown in Figure 4.20 and Figure 4.21.

Image from google earth (Figure 4.23) was used to show the study area for the distribution of silica sand on the northern coastline of Rupert Island. Scattering decomposition from four physical scattering models (double bounce scattering (Figure 4.24), volume scattering (Figure 4.25), surface scattering (Figure 4.26) and helix scattering (Figure 4.27)), the surface scattering is the very clear decomposition to show the silica sand identification compares with others. It was supported by the distribution condition which had flat surface roughness.

This flat surface roughness also supported by the particle size of silica sand grains, which has almost the same size and shape. This slightly rough surface produces strong coherent reflection near the specular direction and a weaker incoherent scatter in other directions.

The result of scattering pattern is strongly dependent on the shape of the illuminated area and exhibits a lobe structure. The incoherent scatter was dealt with in more detail by a perturbation technique rather than the less valid

tangent plane approximation. It was shown that incoherently scattered power from a slightly rough surface of either homogeneous material or a perfectly reflecting interface is directly proportional to the roughness spectral densities.

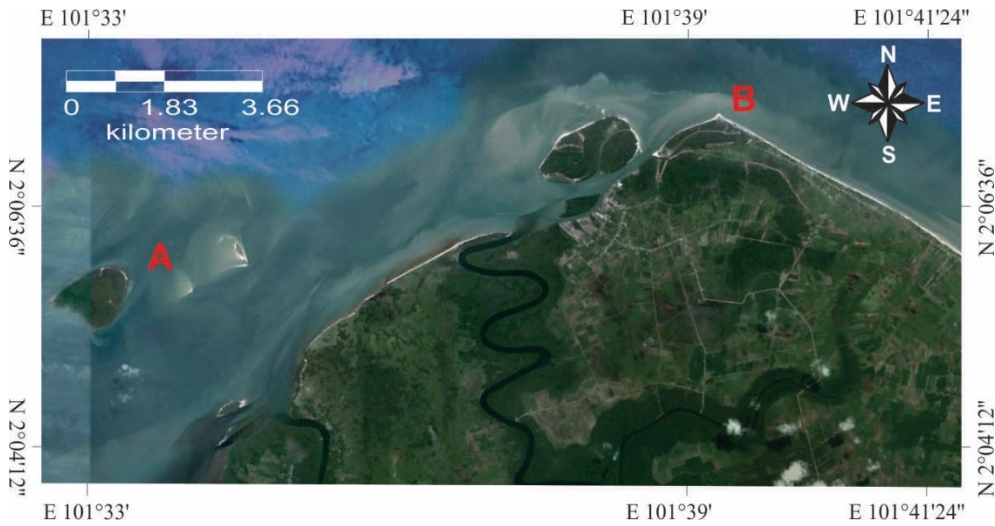


Figure 4.23. Above: Google Earth's Image as the Reference Shown the Silica Sand as White Color along the Northern Coastline of Rupat Island.

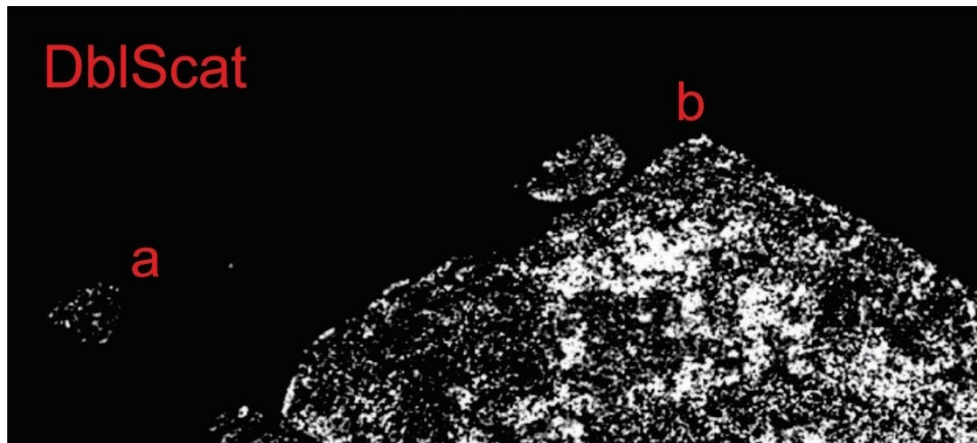


Figure 4.24. Double Bounce Scattering Decomposition on the Northern Coastline of Rupat Island ((a) Beting Aceh location, (b): Tanjung Api location).

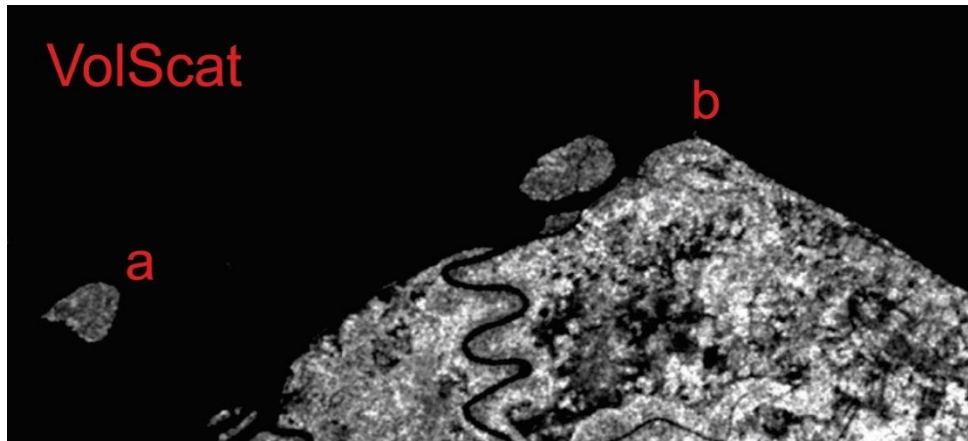


Figure 4.25. Volume Scattering Decomposition on the Northern Coastline of Rupat Island ((a) Beting Aceh location, (b): Tanjung Api location).

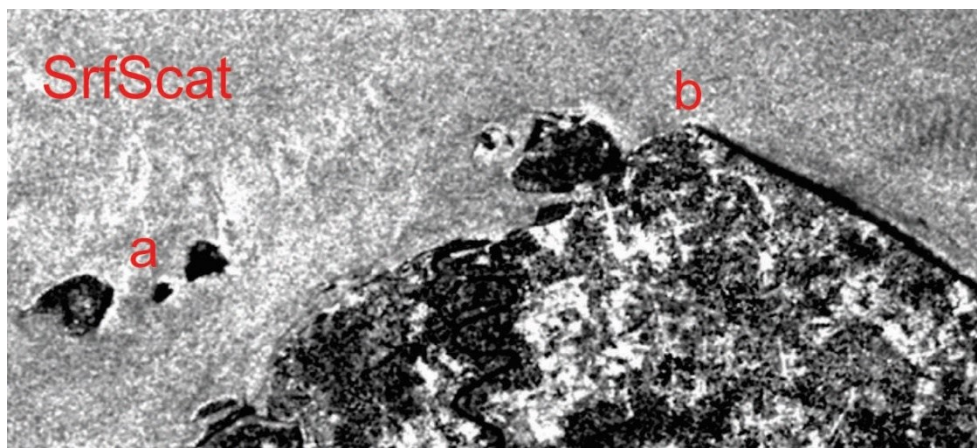


Figure 4.26. Surface Scattering Decomposition on the Northern Coastline of Rupat Island ((a) Beting Aceh location, (b): Tanjung Api location).



Figure 4.27. Helix Scattering Decomposition on the Northern Coastline of Rupert Island ((a) Beting Aceh location, (b): Tanjung Api location).

Backscattering coefficient values of silica sand was calculated starting from -59 dB until -52 dB from the analysis of Double Bounce scattering (see Figure 4.28), Volume scattering (see Figure 4.29), Surface scattering (see Figure 4.30) and Helix scattering (see Figure 4.31), and the very clear is from Surface scattering. These values are given by the surface roughness condition, where the roughness of the surface is slightly rough planar, this condition supported by the grain size of silica sand particles which have almost the same size and shape, which were conducted by using microscopic photograph testing.

All samples from the observation locations shown the properties of sand virtually white and homogeneous by direct observation in the field. It gives the suggestion that the silica sand composition in this area have nearly the same content (see Figure 4.13). The grain size from samples were known by the microscopic photograph testing. Silica sand distributed only on the northern coastline of Rupert Island and spreads around 59 km coverage.

Grain size from the microscopic photograph shown the size of the grains almost with the same size, it relates to the surface condition of the silica sand distribution on the northern coastline of Rupert Island shown the flat surface.

This information helped us to interpret SAR image relating to the surface roughness analysis.

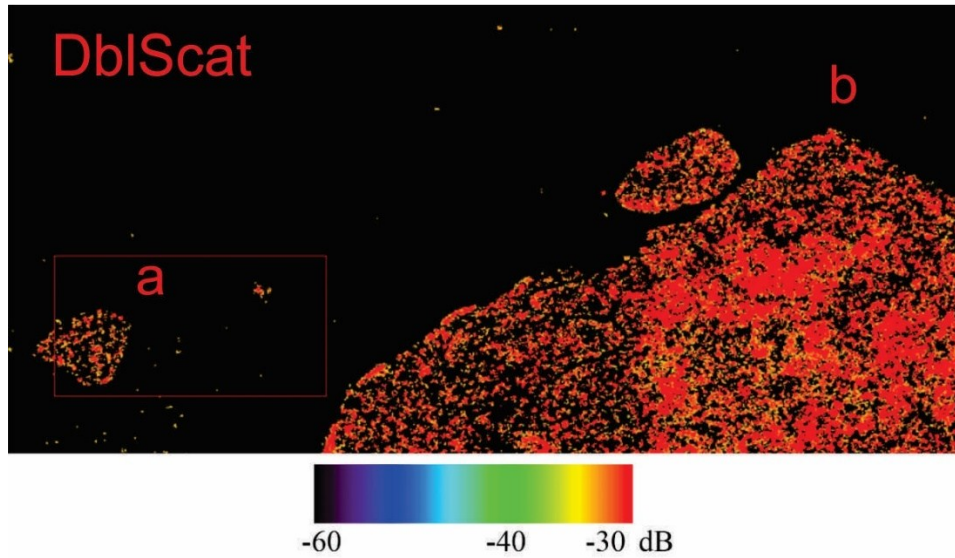


Figure 4.28. Value of Backscattering Coefficient from Polarimetric Decomposition of Double Bounce Scattering on the Northern Coastline of Rupert Island ((a) Beting Aceh location, (b): Tanjung Api location).

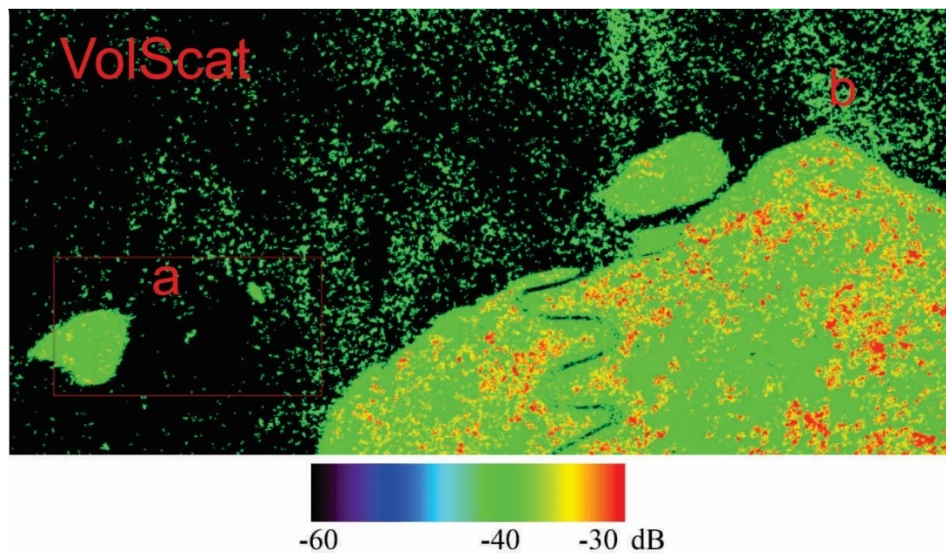


Figure 4.29. Value of Backscattering Coefficient from Polarimetric Decomposition of Volume Scattering on the Northern Coastline of Rupert Island ((a) Beting Aceh location, (b): Tanjung Api location).

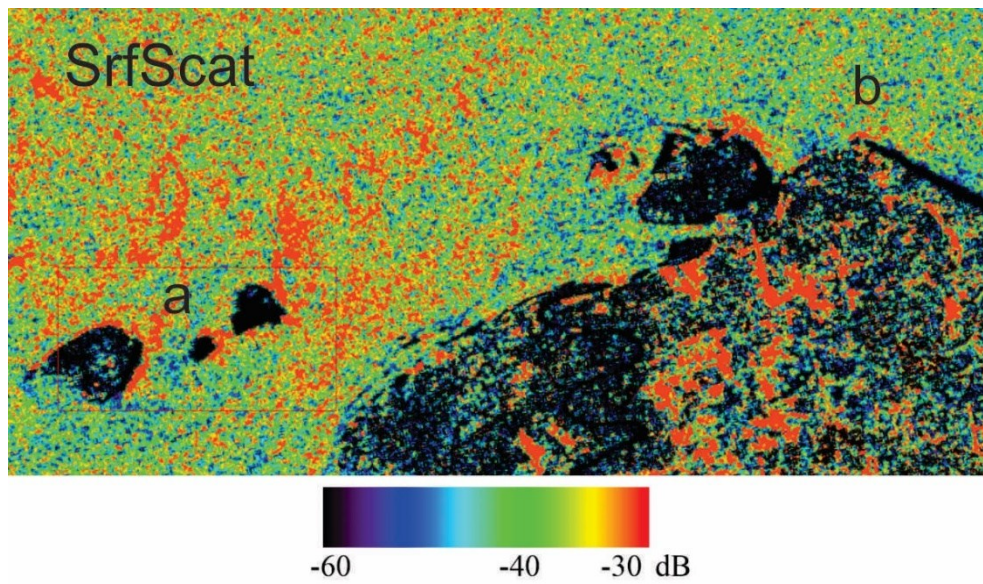


Figure 4.30. Value of Backscattering Coefficient from Polarimetric Decomposition of Surface Scattering on the Northern Coastline of Rupert Island ((a) Beting Aceh location, (b): Tanjung Api location).

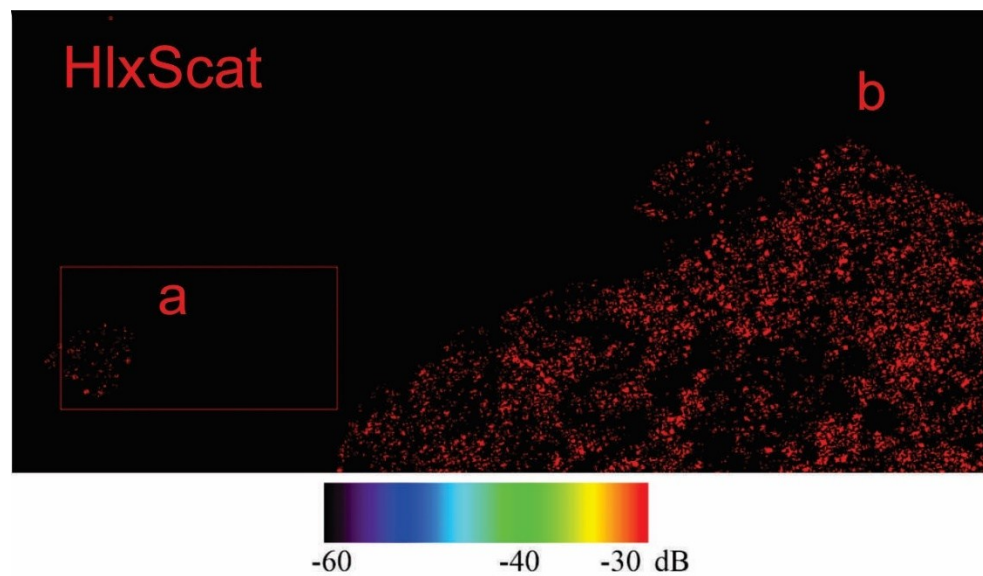


Figure 4.31. Value of Backscattering Coefficient from Polarimetric Decomposition of Helix Scattering on the Northern Coastline of Rupert Island ((a) Beting Aceh location, (b): Tanjung Api location).

To determine the content of silica percentage and the compound of mineral properties, laboratory testing was used for the sand samples obtained from the field survey. The chemical analysis of silica sand samples needs to get the types of compounds/elements, physical properties and percentage content of the compounds/elements.

From laboratory test using X-RF (X-Ray Fluorescence), the abundance of compounds such as SiO_2 , TiO_2 , Al_2O_3 , Fe_2O_3 , MnO , MgO , CaO , Na_2O , K_2O , and P_2O_5 shown from the result of silica sand samples. The result shows the compound of silica (SiO_2) has the high percentage amount above 95% compare to the others mineral in the same samples. The second abundances mineral in these samples is Al_2O_3 , which the average number of it percentages around 0.70% and followed by another mineral as the small number of the samples from northern part of Rupert Island. Based on X-RF test, the percentage content of compounds/minerals shown in Table 4.1 for five locations of observation (Beting Aceh, Tanjung Api, Teluk Rhu, Tanjung Punai and Tanjung Lapin).

Refer to the sedimentary provenance and its association with sedimentary transportation agent [38], [40], [41], sedimentary grain shape and grain size characteristic of silica sand on the northern coastline of Rupert Island are rounded and the shape size is almost same. These mean silica sand was transported from far location / source. This analysis also supported that silica sand was not produced by this island bedrock.

4.4 Thickness estimation of silica sand layer

Based on the ground survey or field data, and the assumption that silica sand layer as the surface / top layer profile from the different classes in the study area, the study area is composed of two layers; 0 to 70 cm and below 70 cm is the surface of the bedrock, also the assumption that the thickness of the bedrock is infinite, a multi-layer model has been conducted to analyze the

relationship between the backscattering coefficient (σ^0) and the total thickness of silica sand layer (ξ_s). Since the research main objective is to estimate the total thickness of silica sand layer on the northern coastline of Rupert Island, and declared that the physical properties of bedrock and silica sand layers are comparable, the averages of the backscattering coefficients (σ^0) for both layers class were obtained. Figure 4.32 shows the relationship between the average backscattering coefficient (σ^0) and layer thickness, which was obtained from the multilayer modeling analysis.

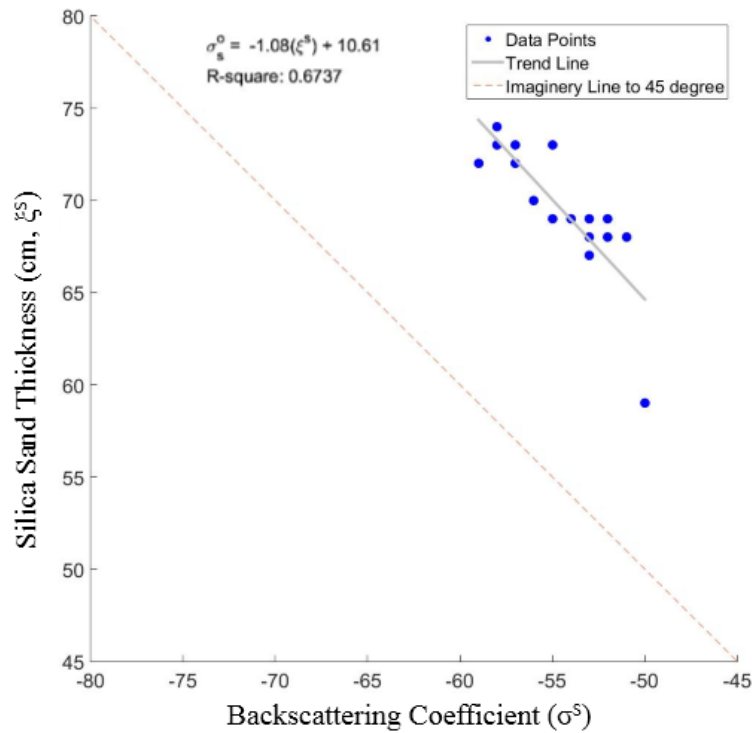


Figure 4.32. Relationship between silica sand layer thickness and backscattering coefficient.

Backscattering coefficients has been derived and plotted from ALOS PALSAR image on Figure 4.32, and the average, maximum and minimum thickness of each class was obtained. Table 4.3 shows the layer thickness estimation at Beting Aceh location is 72 cm, 68 cm, 69 cm, and the average thickness estimation is 69.67 cm. Tanjung Api location has 68 cm, 70 cm, 69

cm of the layer thickness, and the average thickness estimation is 69 cm. Silica sand thickness estimation at Teluk Rhu is 73 cm, 59 cm, 73 cm, and the average thickness estimation is 68.33 cm. Tanjung Punai location has 72 cm, 67 cm, 68 cm of the layer thickness, and the average thickness estimation is 69 cm. Silica sand thickness estimation at Tanjung Lapin is 74 cm, 69 cm, 73 cm, 69 cm and the average thickness estimation is 71.25 cm. The total average of layer thickness estimation from the distribution of silica sand on the northern coastline of Rupert Island is 69.56 cm.

The comparison estimation values of the layer thickness from satellite calculation with the field data measurement can be seen in Table 4.3, the layer thickness for the different silica sand type is comparable, where field data revealed that the minimum thickness for Beting Aceh location is 70 cm and followed by 75 cm and 75 cm thickness for other field measurements at this location with the average thickness is 73.33 cm.

The minimum thickness for Tanjung Api location is 73 cm and followed by 76 cm and 76 cm thickness for another field measurement at this location with the average thickness is 75 cm.

The minimum thickness for Teluk Rhu location is 65 cm and followed by 75 cm and 78 cm thickness for another field measurement at this location with the average thickness is 72.67 cm.

The minimum thickness for Tanjung Punai location is 75 cm and followed by 75 cm and 75 cm thickness for another field measurement at this location with the average thickness is 75 cm.

The minimum thickness for Tanjung Lapin location is 75 cm and followed by 75 cm, 76 cm and 76 cm thickness for another field measurement at this location with the average thickness is 75.75 cm.

The total average of layer thickness from field measurement of the silica sand distribution on the northern coastline of Rupert Island is 74.44 cm.

All of the parameter measurements have been derived by using the dielectric constant value from each samples of 16 locations in this study area (Figure 4.33 until Figure 4.48).

Table 4.3. Table of dielectric constant of sample, backscattering coefficient Value from ALOS PALSAR and field, average error, average ratio and silica sand layer thickness estimation from study area at northern coastline of Rupat Island.

Location		Dielectric Constant	Back-scattering coefficient of ALOS PALSAR	Back-scattering coefficient of field	Ratio	Layer thick-ness esti-mation (centi-meter)	Field layer thickness mea-surement (centi-meter)
Beting Aceh	1	2.972	-59	-53	1.11	72	75
	2	2.359	-52	-49	1.06	68	70
	3	2.259	-54	-50	1.08	69	75
						Avg: 69.67	Avg: 73.33
Tanjung Api	4	2.359	-51	-49	1.04	68	73
	5	2.159	-56	-51	1.1	70	76
	6	2.259	-53	-50	1.06	69	76
						Avg: 69	Avg: 75
Teluk Rhu	7	2.891	-58	-56	1.06	73	75
	8	2.362	-50	-42	1.19	59	65
	9	2.892	-55	-54	1.02	73	78
						Avg: 68.33	Avg: 72.67
Tanjung Punai	10	2.972	-57	-53	1.08	72	75
	11	2.421	-53	-48	1.04	67	75
	12	2.359	-53	-49	1.08	68	75
						Avg: 69	Avg: 75
Tanjung Lapin	13	2.821	-58	-55	1.05	74	77
	14	2.259	-52	-50	1.04	69	76
	15	2.891	-57	-56	1.02	73	75
	16	2.259	-55	-50	1.1	69	75
						Avg: 71.25	Avg: 75.75
Average			-54.56	-50.94	1.07	69.56	74.44

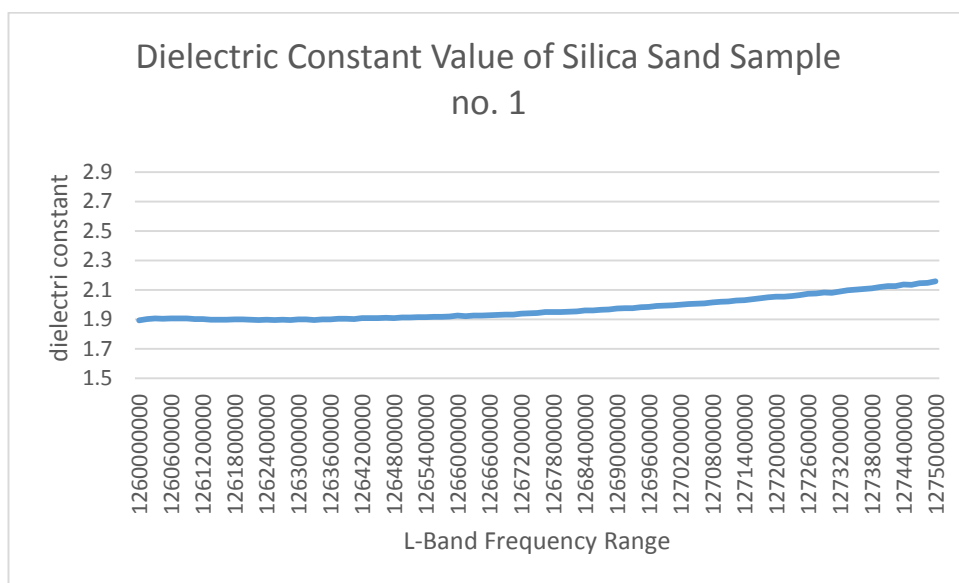


Figure 4.33. Dielectric Constant Value of Silica Sand Sample no. 1 in the Beting Aceh Area.

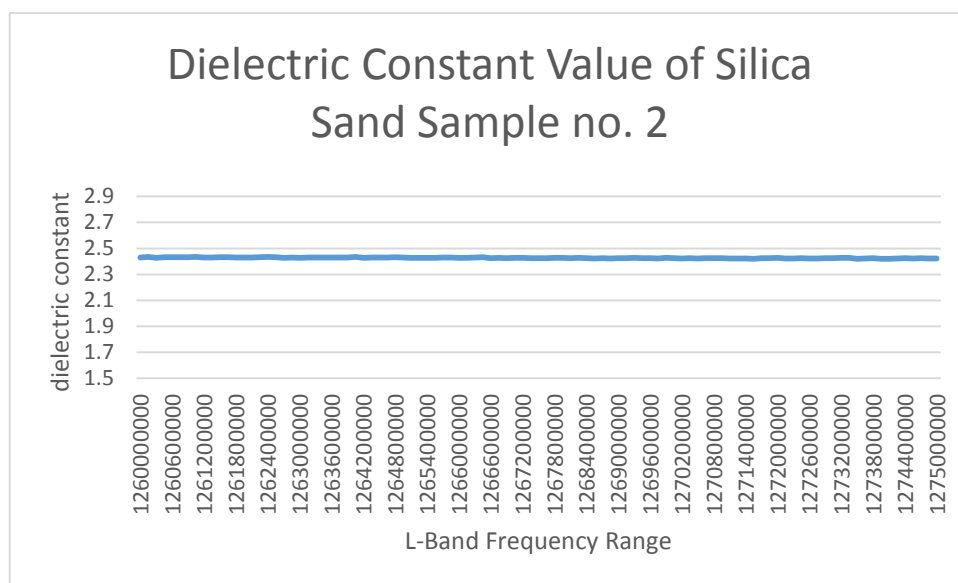


Figure 4.34. Dielectric Constant Value of Silica Sand Sample no. 2 in the Beting Aceh Area.

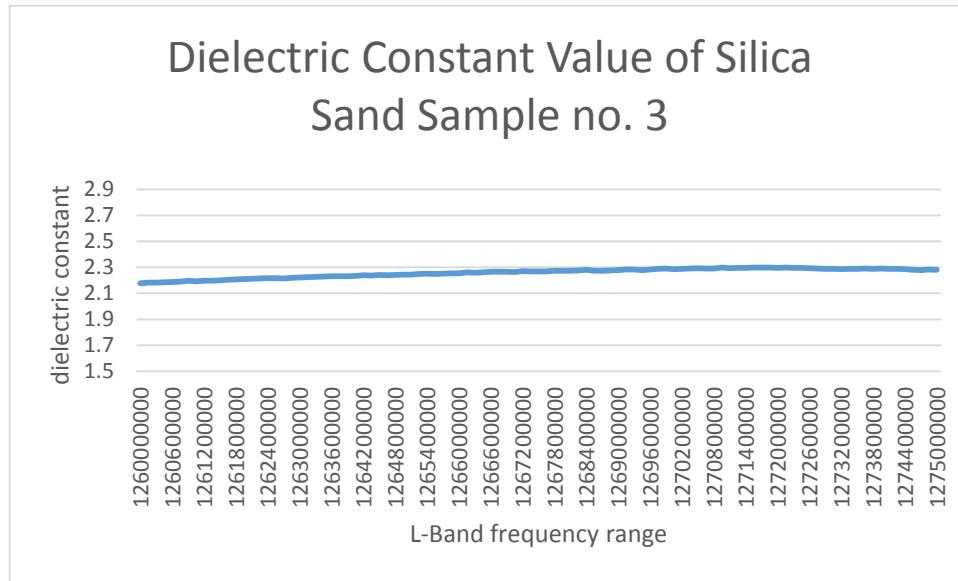


Figure 4.35. Dielectric Constant Value of Silica Sand Sample no. 3 in the Beting Aceh Area.

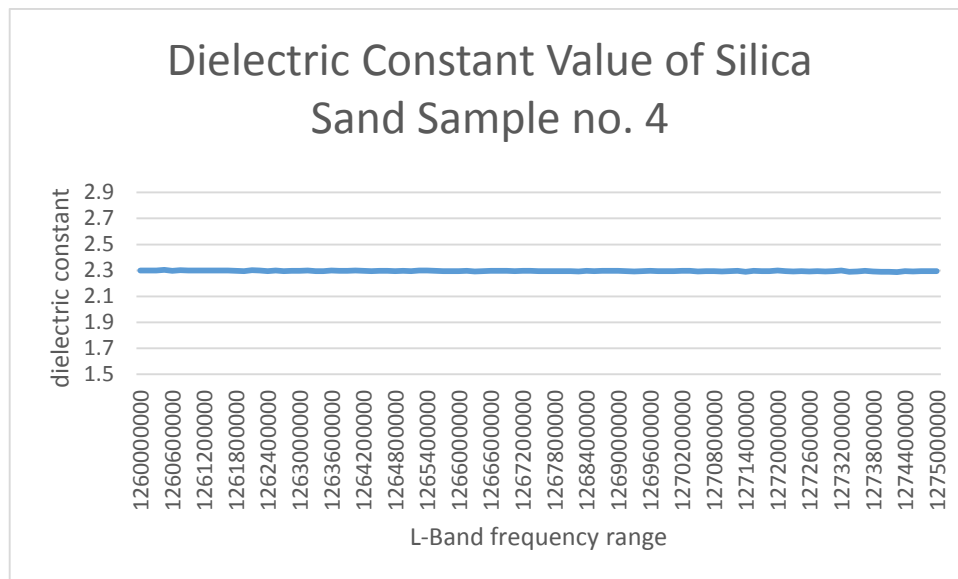


Figure 4.36. Dielectric Constant Value of Silica Sand Sample no. 4 in the Tanjung Api Area.

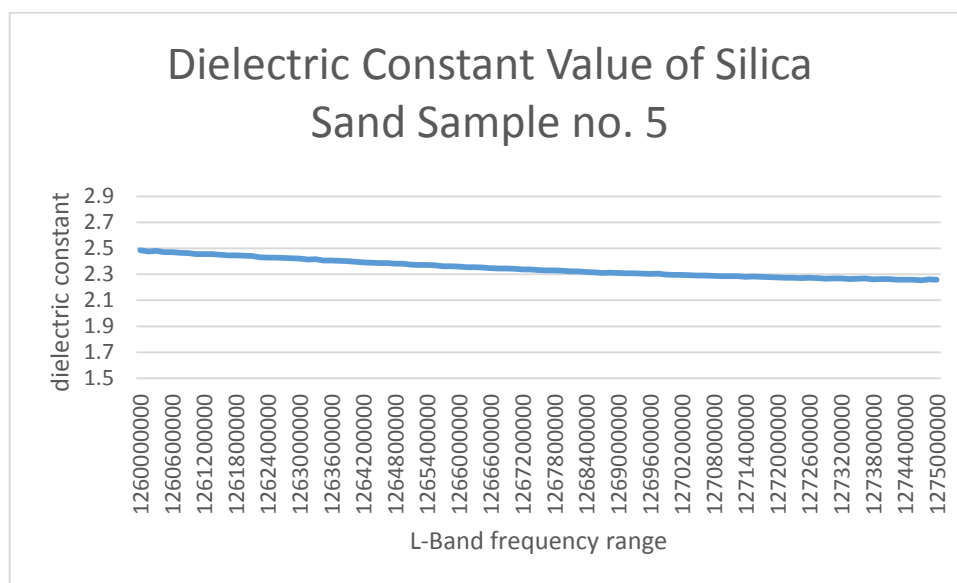


Figure 4.37. Dielectric Constant Value of Silica Sand Sample no. 5 in the Tanjung Api Area.

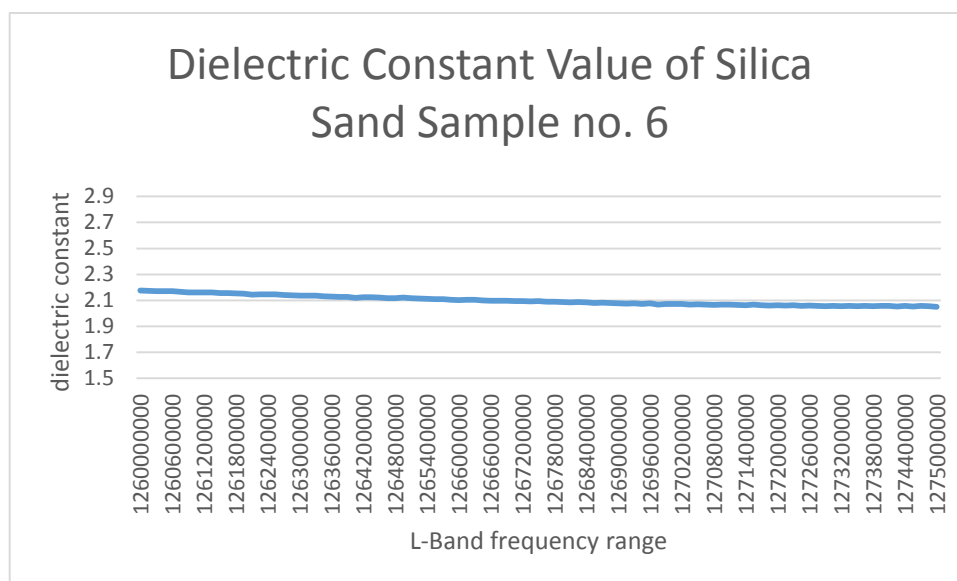


Figure 4.38. Dielectric Constant Value of Silica Sand Sample no. 6 in the Tanjung Api Area.

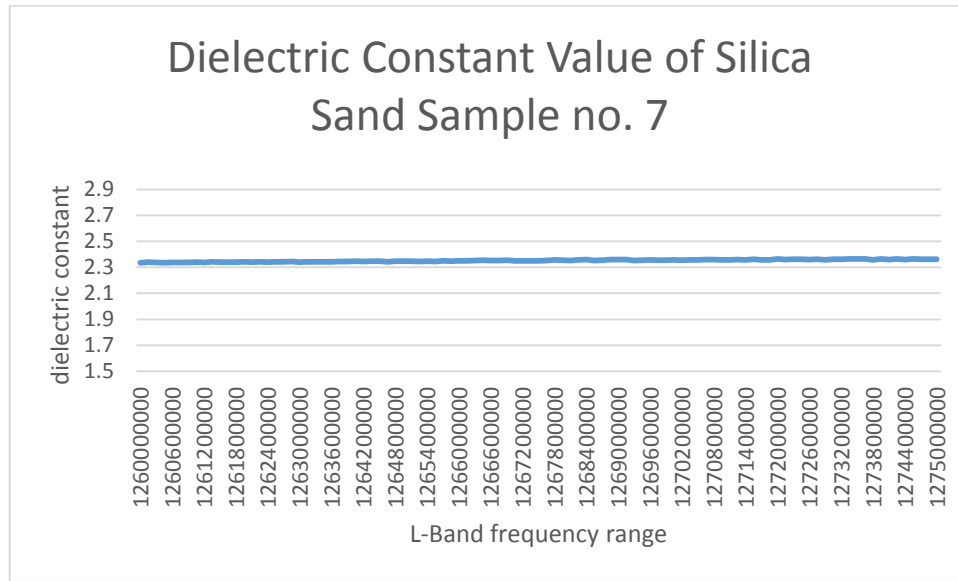


Figure 4.39. Dielectric Constant Value of Silica Sand Sample no. 7 in the Teluk Rhu Area.

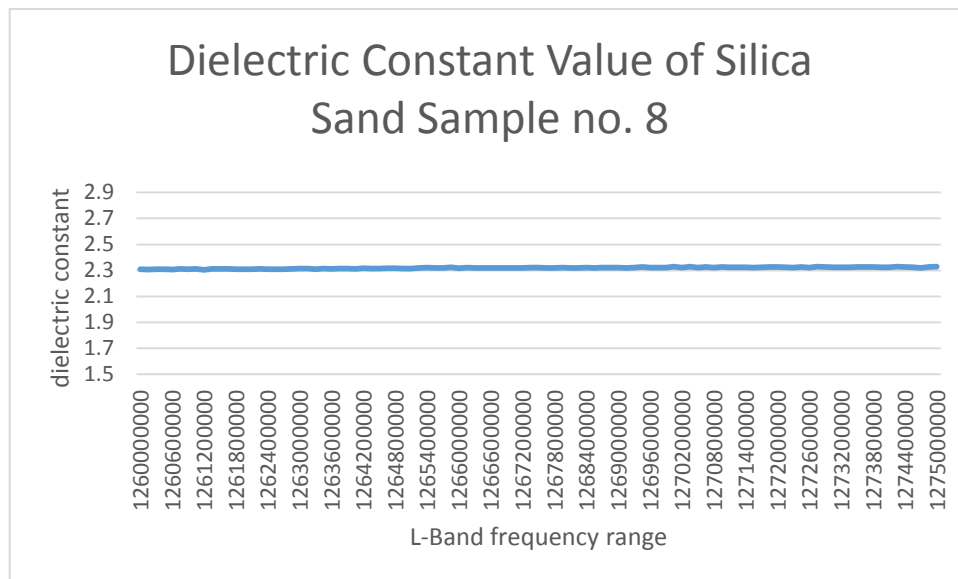


Figure 4.40. Dielectric Constant Value of Silica Sand Sample no. 8 in the Teluk Rhu Area.

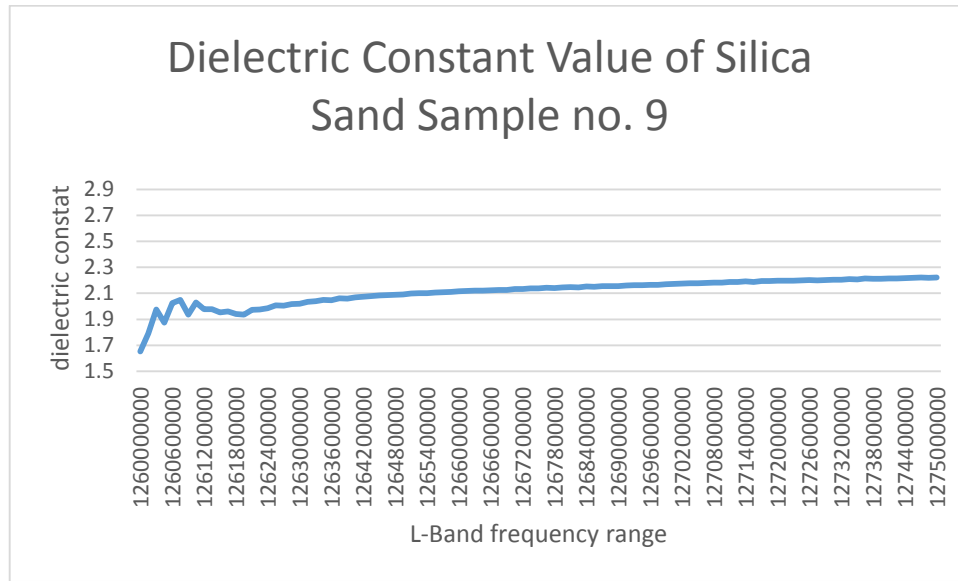


Figure 4.41. Dielectric Constant Value of Silica Sand Sample no. 9 in the Teluk Rhu Area.

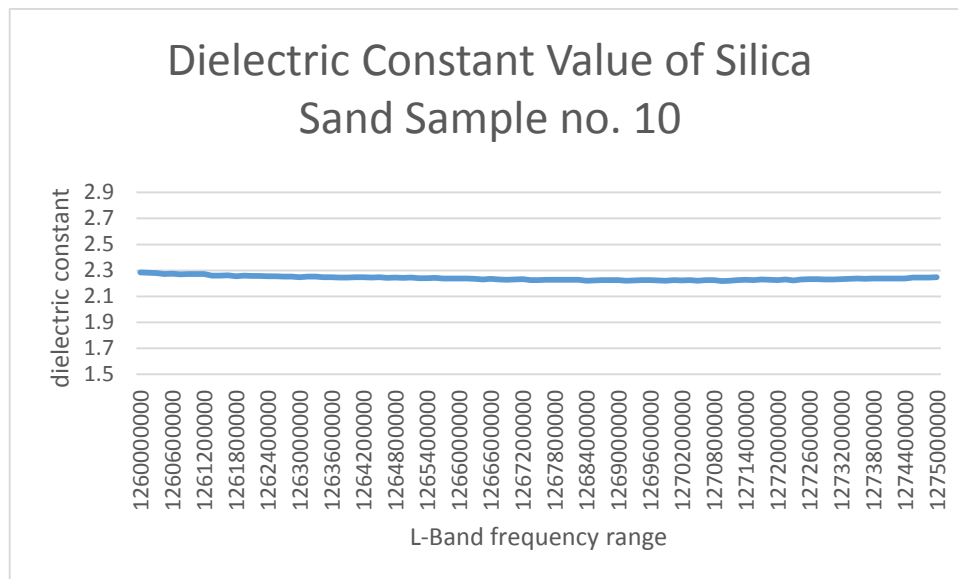


Figure 4.42. Dielectric Constant Value of Silica Sand Sample no. 10 in the Tanjung Punai Area.

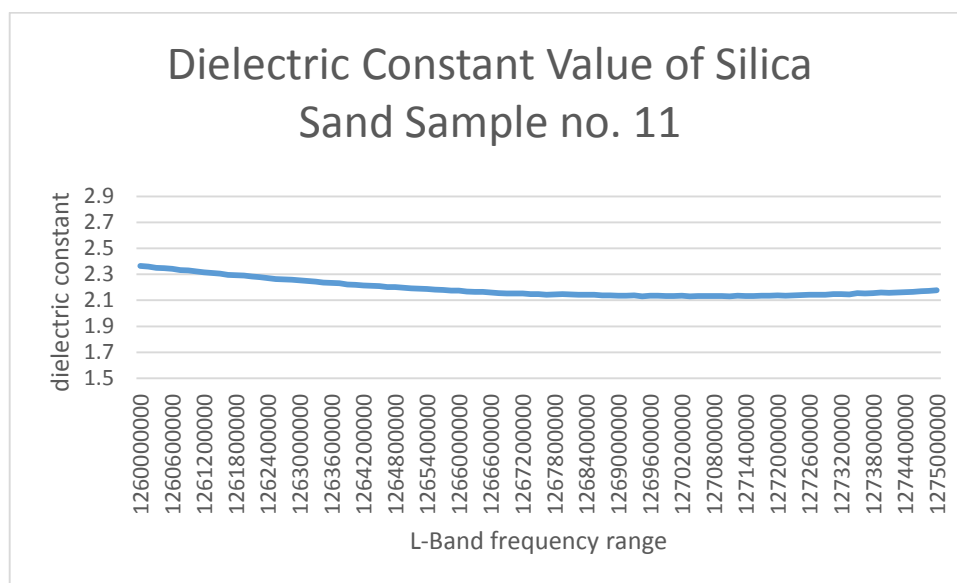


Figure 4.43. Dielectric Constant Value of Silica Sand Sample no. 11 in the Tanjung Punai Area.

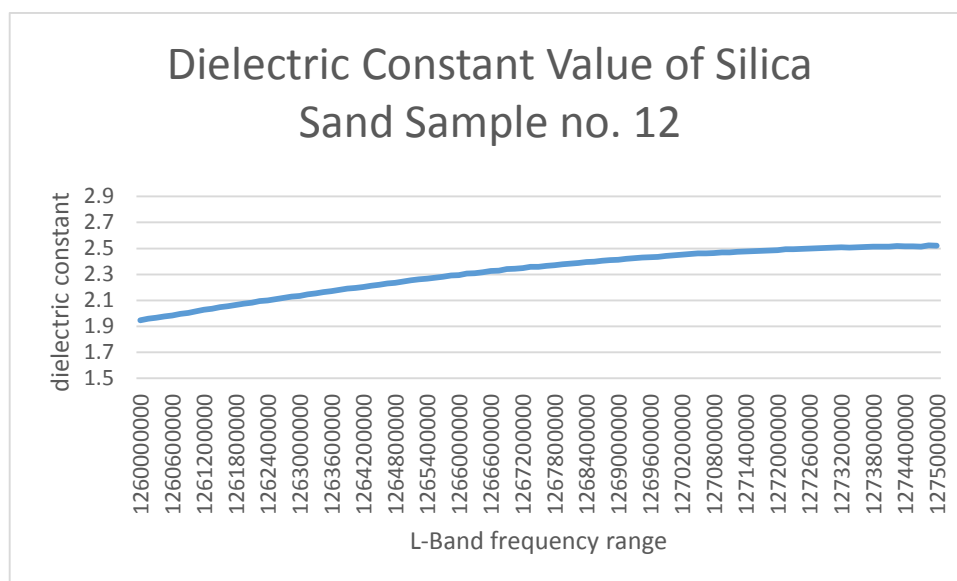


Figure 4.44. Dielectric Constant Value of Silica Sand Sample no. 12 in the Tanjung Punai Area.

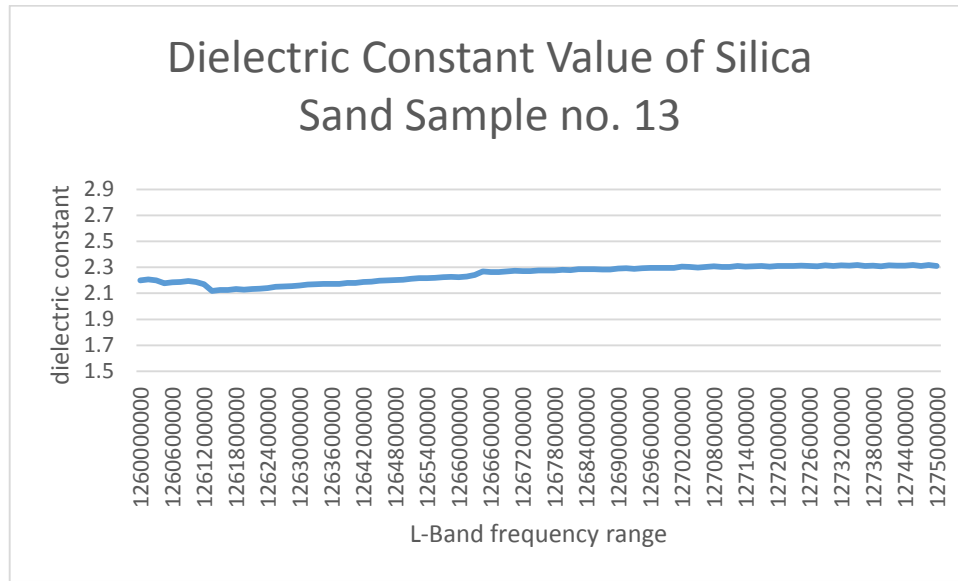


Figure 4.45. Dielectric Constant Value of Silica Sand Sample no. 13 in the Tanjung Lapin Area.

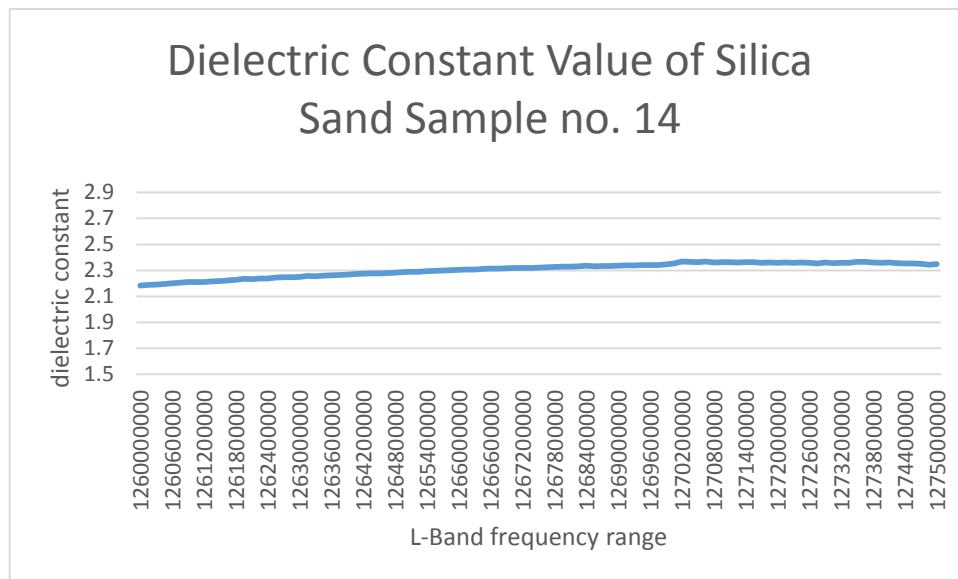


Figure 4.46. Dielectric Constant Value of Silica Sand Sample no. 14 in the Tanjung Lapin Area.

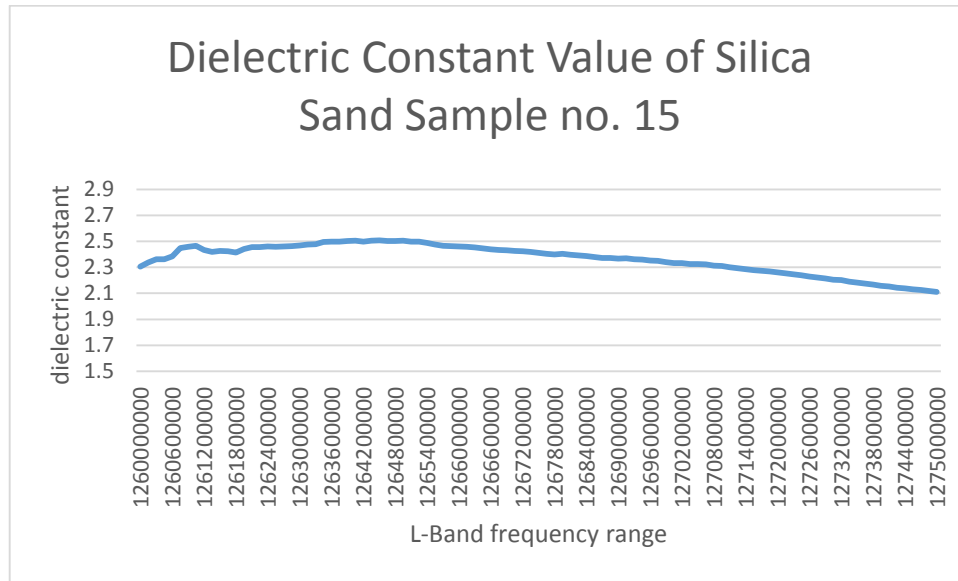


Figure 4.47. Dielectric Constant Value of Silica Sand Sample no. 15 in the Tanjung Lapin Area.

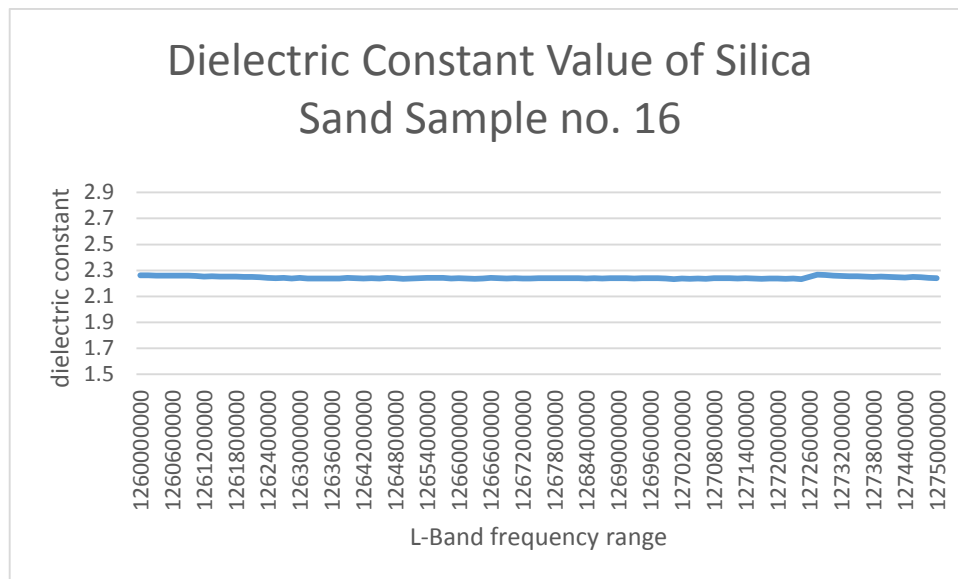


Figure 4.48. Dielectric Constant Value of Silica Sand Sample no. 16 in the Tanjung Lapin Area.

From Table 4.3, the differentiation value of silica sand layer thickness from satellite estimation and field measurement can be calculated. For Beting Aceh

location, the average of the layer thickness different value is 5.33 cm. For Tanjung Api location, the average of the layer thickness different value is 6 cm. For Teluk Rhu location, the average of the layer thickness different value is 4.34 cm. For Tanjung Punai location, the average of the layer thickness different value is 6 cm. For Tanjung Api location, the average of silica the thickness different value is 4.5 cm.

The total average between layer thickness estimation from satellite and field layer thickness measurement of the silica sand distribution on the northern coastline of Rupert Island is 72 cm. Layer thickness estimation from satellite compares to the field data measurement shown there was a small different between this measurement; 4.88 cm. This differentiation caused by surface roughness, multiple scatterings, multiple objects at the same area (which mean has multiple dielectrics constant), water content, humidity, weather condition, differentiation of incidence angle between field and satellite image measurement.

Figure 4.49 shows relationship between silica sand thickness estimated using satellite data and measured from field with R^2 0.6722, which represents significant agreement between silica sand thicknesses estimated using satellite data and measured from field.

Research on this study area shows that silica sand distribution, and its thickness estimation influenced by the humidity and water content. This area, which is a coastline area, has more water content that can block the backscattered wave to the microwave satellite. This research also compares with previous research [42] and shows that the different backscattering effect between those is different. For dried area, microwave signal, especially the penetration of L-band SAR is deeper than the wet area. In the assumption that bedrock of silica sand layer on this northern coastline of Rupert Island is the wet area, this analysis limited to the area that has wetter.

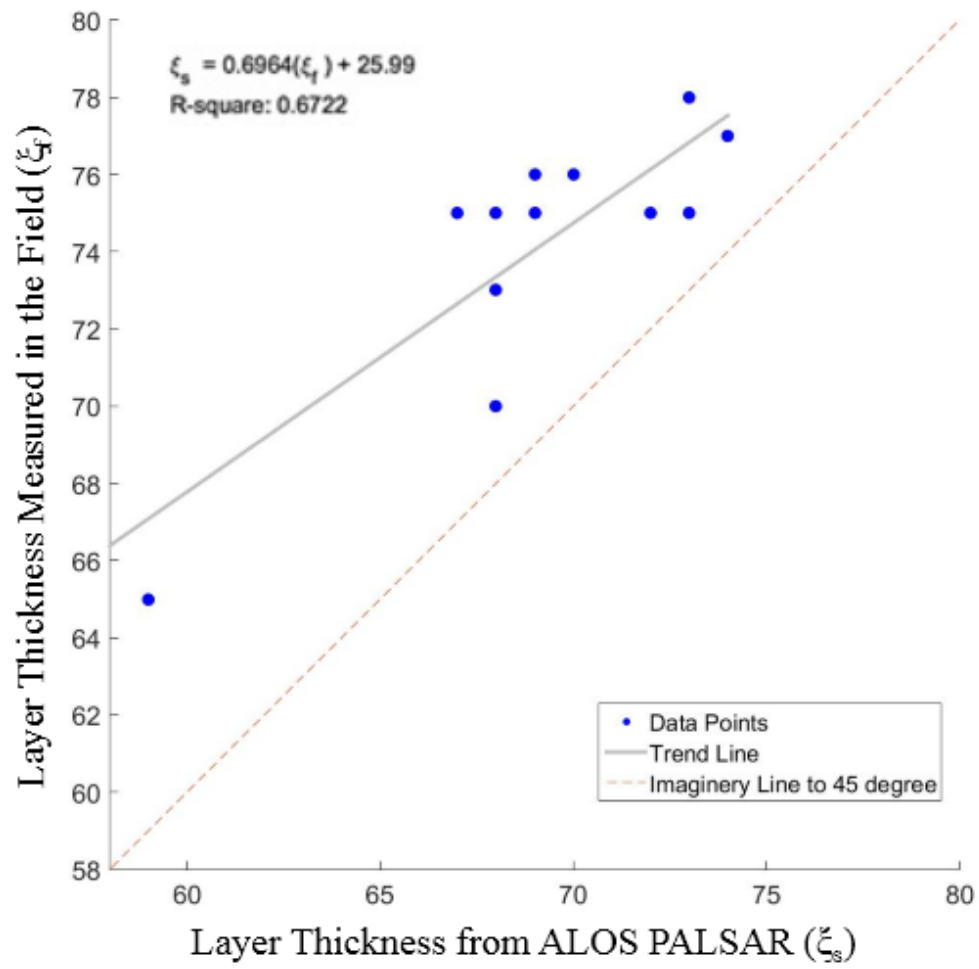


Figure 4.49. Relationship between silica sand thickness from satellite and field measurement.

5 CONCLUSION AND FUTURE PLANNING

5.1 Conclusion

Currently, Silica sand is a concern as the one alternative to be used as a base for renewable energy. Silica sand can be used as raw material to produce renewable energy as the basic material for making solar panels in the example. In addition, the use of silica sand industry is to make tools such as ceramic and the glass industry. Silica sand is also currently used as the filter in the oil and gas industry. The problem that arises now is how to be able to find the source of silica sand, which is actually widely spread in nature. By using remote sensing techniques, particularly the technique of microwave remote sensing SAR, facilitate the work to find the distribution of silica sand in nature.

To determine the distribution of silica sand, ground survey required in the field to carry out the geological mapping. Detailed geological mapping is required to obtain information of silica sand distribution, which contains the sample, the pattern and the width of silica sand distribution. In addition, determining the composition of silica sand, laboratory analysis is necessary. Laboratory analysis is very important to find out the identity information of the silica content. For example, by using a microscopic photograph, it can be seen the grain shape, size and color of silica sand sample. From the analysis of microscopic photograph, grain shape of silica sand in the research area shows almost in round-shape.

This representation form, in the science of sedimentology, gives meaning that the sand grains came far away from the source, this analysis gives the conclusion that the source of silica contained in this research area is not from the in situ of Rupert island bedrock. Grain size obtained is also evidence that the silica sand has almost the same size, it shows that the grain of silica sand has experienced a lot of sorting process as a result of a long transport process.

This condition supports the conclusion that the source of silica sand is far from this island and also supports that silica sand comes not from the island's bedrock. The next in terms of color was observed, the color of silica sand in this area is white. The natural condition of the real silica sand generally is dirty and not white. It is caused by the mixing with other minerals that were dominated by the iron and aluminum minerals, where the iron minerals will give effect to a brownish color and aluminum effects reddish color. From the appearance color indicated, it concludes that the silica content is high, and it also has been supported by the percentage of silica content by using the technique of X-Ray Fluorescence (X-RF) and X-Ray Diffraction (X-RD).

In this study, we were working the distribution and thickness estimation of silica sand in the northern coastline of Rupert Island. The result shown high silica content above 95%. The origin of the silica sand is not from the Rupert Island bedrock, but it came from the Malacca Strait which brought the sediment source.

Full polarimetry SAR data helped this research to interpret land information. In this study, distribution of silica sand on the northern coastline of Rupert Island was studied as the interesting topic. From ALOS PALSAR full polarimetry data the distribution of silica sand in this island was identified and compared with field data measurement and sample analysis. Two adjacent scenes of ALOS PALSAR full-polarimetry data were used, the first full polarimetry ALOS PALSAR scene acquired on May 16, 2010, and the second were acquired on April 03, 2011. Using the modified formula,

identification of silica sand can be measured with small error between satellite and field. It caused by surface roughness, multiple scatterings, multiple objects at the same area (which mean has multiple dielectrics constant), water content, humidity, weather condition, differentiation of incidence angle between field and satellite image measurement.

Scattering decomposition from four physical scattering models (Double Bounce scattering, Volume scattering, Surface scattering and Helix scattering) shows the surface scattering is the clearest decomposition for the silica sand identification compares with other decompositions. From surface scattering, backscattering coefficient value of silica sand was calculated starting from -59 dB until -52 dB. These values were given by the surface roughness condition, where slightly rough planar, this condition supported by the grain size of silica sand particles that have almost the same size and shape, that were conducted by using microscopic photograph testing. Identification of silica sand existence traced by backscattering coefficient. From both of backscattering coefficient of satellite and sample analysis, the average error, average ratio was calculated.

5.2 Contribution

The high content of silica can be utilized for the use of industrial raw materials. From the results obtained, the points can be determined as the potential for mining activities.

In addition for mining activities, the planning for this activity needs detail calculation carefully. Besides of the mining activities, the other potential for this area is the development of the tourism industry, because the island has a white-sand beach that stretches along the northern coastline. The mining industry and tourism can be combined in an appropriate setting because the northern coastline of Rupert Island is very long.

This research is useful to know the distribution and the thickness of the silica sand in this study area. Other than that this research will be a guide to another research oriented to the distribution and depth of objects contained in the earth's surface.

5.3 Future Planning

The research presented in this thesis may be extended in a variety of ways. Following is a list of some possible works:

1. Identification and calculation of many possible areas that have economic mineral study. The currently situation of economical mineral exploration still use traditionally geological mapping technique, it means the traditionally technique will cost expensively and take a long time which are not effective and efficient. By using the new technique that we have developed, we propose a new technique that make very simple and large cover of exploration area.
2. By using the technique that we have been developed, we will try for the close future research regarding the contamination area in mainland caused by the oil spill in the exploitation area. Riau province is the famous province that produce oil and gas industry, it has been started since 50 years ago. This industry also give negative effect to the environment especially the location nearby the exploitation area. This technique will help us to interpret the contamination area which will cover the distribution of contamination by oil spill and the thickness of the contamination area, especially in an open area.
3. The development of this technique may be completed for the next research to get more detail information regarding thickness estimation of any objects beneath the earth surface. This technique needs more

development to get more detail and precise interpretation especially for the subsurface mapping beneath the earth surface.

4. This work initially began as a study to design the technique to build the model of thickness estimation and the distribution of an object by identify its properties characteristic especially from its dielectric constant value. The physical characteristic will help the interpretation to identify of any objects. For the future research, it will help to analyse of a focus object to identify and calculation for the large area, especially for the geological condition.
5. Analysis on the polarimetric characteristic will help on the interpretation of the object changes by the time periodic. For an example, the change of an object can be identified by the time. For our case that has been done, we observed the bridge deflection and the result shows the deflection accurately in centimetre changes. For the future, we will develop this technique in advance step to get the detail change on the object character by the time.
6. In geological mapping, the change of any geological object that affected by the time is needed to be observed. This technique also help us to solve the geological problem in large scale. Especially to identify the distribution of mineral. This technique made the geological mapping work become easily, by using this technique identifying mineral appearance mineral is very easy and it very helpful for the geological mapping.

6 REFERENCES

- [1] N. Wicaksono, “Survei Potensi Pasir Kuarsa di Daerah Ketapang Propinsi Kalimantan Barat,” *Jurnal Sains dan Teknologi Indonesia*. **11**(2), 126-132 (2012).
- [2] J. R. Brown. 2000. Foseco Ferrous Foundryman's Handbook (Eleventh Edition), Chapter 12 Sands and Green Sand, 146–166.
- [3] Kausarian, H., Abdul Rahim Shamsudin, Yuniarti Yuskar. 2014. Geotechnical and Rock Mass Characterization Using Seismic Refraction Method At Kajang Rock Quarry, Semenyih, Selangor Darul Ehsan. *Journal of Ocean, Mechanical and Aerospace-Science and Engineering*, **13**. 12-17
- [4] Kausarian, H, 2015. Rock Mass, Geotechnical and Rock Type Identification Using SASW and MASW Methods at Kajang Rock Quarry, Semenyih, Selangor Darul Ehsan. *Journal of Ocean, Mechanical and Aerospace -Science and Engineering-*, Vol.13. 7-12.
- [5] Ghalya A.E, Ergüdenlera A, Lauferb E. 1994. Study of agglomeration characteristics of silica sand-straw ash mixtures using scanning electronic microscopy and energy dispersion X- ray techniques. *Bioresource Technology* Volume 48, Issue 2, 127–134.
- [6] S. Hasdemir, A. Tuğrul, M. Yılmaz. (2016). The effect of natural sand composition on concrete strength, *Construction and Building Materials* **112**: 940-948.
- [7] I. V. Konstantinos, C. Georgios, P. Spiridon, P. B. Nikolas, 2014. Market Developments and Industrial Innovative Applications of High Purity

Quartz Refines. *Procedia Economics and Finance*, International Conference on Applied Economics, ICOAE 2014, Volume 14, 2014: 624–633.

[8] I. N. Murthy et al. 2016. Investigations on Physical and Chemical Properties of High Silica Sand, Fe-Cr Slag and Blast Furnace Slag for Foundry Applications, *Procedia Environmental Sciences*. **35**, 583-596.

[9] S. Rafat, C. Navneet, 2011. Use of silicon and ferrosilicon industry by-products (silica fume) in cement paste and mortar, *Resources, Conservation and Recycling*, Volume 55, Issue 8, June 2011: 739-744.

[10] W. Rikke, F. Henrik, M. K. Afsoon, B.S Johan, S. Jesper, L. K. P. Mette. 2010. Development of early diagenetic silica and quartz morphologies —Examples from the Siri Canyon, Danish North Sea. *Sedimentary Geology*, Volume 228, Issues 3–4, 151–170.

[11] G. Spagnoli et al. 2015. Estimation of the compression and tension loads for a novel mixed-in-place offshore pile for oil and gas platforms in silica and calcareous sands, *Journal of Petroleum Science and Engineering*. **136**, 1-11.

[12] Kausarian, H, Mursyidah, W. Sugeng, 2013. Silica Sand Potency of Bukit Pelintung as Base Material of Solar Cell. *Journal of Ocean, Mechanical and Aerospace -Science and Engineering-*, Vol.2, December 2013: 20-24.

[13] Kausarian, H, J. T. S Sumantyo, H. Kuze, B. E. P. Dewandra. 2015. Mapping of the oldest layer exposure at the top layer of Riau bedrock using Alos Palsar Mosaic 25M-Resolution data. *Proceeding of The 58th Spring International Conference of the Remote Sensing Society of Japan*. 72-75.

[14] Kausarian, H, J. T. S. Sumantyo, H. Kuze, 2015. Physical and dielectric properties measurement to identify the distribution of silica sand using alos/palsar full polarimetry on the northern coastline of rupa island, indonesia.

Proceeding The 23rd CEReS International Symposium, Chiba University, Japan. 24-27.

[15] Kausarian, H, J. T. S. Sumantyo, H. Kuze, 2016. Identification of Silica Sand Distribution on the northern Coastline of Rupert Island Using ALOS/PALSAR Full Polarimetry Data. *Proceeding International Symposium on Remote Sensing 2016*. 101-104.

[16] N. R. Cameroon, W. Kartawa, S. J. Thompson, 1982. Geological Map Sheet of Dumai and Bagan Siapi-api, Scale 1:250.000. Centre for Geology Research and Development, Bandung.

[17] Yarmanto, Aulia. (1998). Seismic Expression of Wrench Tectonics in the Central Sumatra Basin, *Proceeding 17th IAGI Annual Convention*.

[18] W. C. Dawson, Yarmanto, U. Sukanta, D. Kadar, S. B. Sangree. 1997. Regional Sequence Stratigraphic Correlation Central Sumatra, PT Caltex Pacific Indonesia, Rumbai.

[19] M. Shimada, 2010. Ortho-rectification and slope correction of SAR data using DEM and its accuracy evaluation. *IEEE Journal of Selected Topics in Applied Earth Observations and Remote Sensing*, Vol. 3. No. 4, pp. 657-671.

[20] T. Shiraishi, T. Motohka, R. B. Thapa, M. Watanabe, M. Shimada, 2014. Comparative assessment of supervised classifiers for land use-land cover classification in a tropical region using time-series palsar mosaic data. *IEEE Journal of Selected Topics in Applied Earth Observations and Remote Sensing*, Vol. 7, No. 4, pp. 1186-1199.

[21] R. B. Thapa, M. Watanabe, T. Motohka, M. Shimada, 2015. Potential of high-resolution ALOS-PALSAR mosaic texture for aboveground forest carbon tracking in tropical region. *Remote Sensing of Environment*, Vol. 160, pp. 122-133.

- [22] R. Gens, 2010. Remote sensing of coastlines: detection, extraction and monitoring. *International Journal of Remote Sensing*, Vol. 31, No. 7, pp. 1819-1836.
- [23] F. Baselice, G. Ferraioli, 2013. Unsupervised coastal line extraction from SAR images. *IEEE Geoscience and Remote Sensing Letters*, Vol. 10, No. 6, pp. 1350-1354.
- [24] M. K. Ghosh, L. Kumar, C. Roy, 2015. Monitoring the coastline change of Hatiya Island in Bangladesh using remote sensing techniques. *ISPRS Journal of Photogrammetry and Remote Sensing*, Vol 101, pp. 137-144.
- [25] S. S. J. Tetuko, R. Tateishi, N. Takeuchi, 2003. Estimation of Burnt Coal Seam Thickness in Central Borneo Using JERS-1 SAR Data. *International Journal Remote Sensing*, Vol. 24, pp. 3119 – 3136.
- [26] S. S. J. TETUKO, R. TATEISHI, N. TAKEUCHI, 2003. A physical method to analyse Estimating topsoil thickness in Jordan using SAR data 3881 scattered waves from burnt seam and its application to estimate thickness of fire scars in central Borneo using L-band SAR data. *International Journal of Remote Sensing*, 24, 3119–3136.
- [27] P. Mishra, G. Shivangi, S. Dharmendra, 2013. An impedance based approach to determine soil moisture using radarsat-2 data. In *IEEE International Geoscience and Remote Sensing Symposium-IGARSS*, 21-26 July 2013, Melbourne, Australia. Edited by Melba Crawford. IEEE, Piscataway, NJ. pp. 2724-2727.
- [28] D. Kachelriess, M. Wegmann, M. Gollock, N. Pettorelli, 2014. The application of remote sensing for marine protected area management. *Ecological Indicators*, Vol 36, pp. 169-77.

- [29] X. Monteys, P. Harris, S. Caloca, C. Cahalane, 2015. Spatial Prediction of Coastal Bathymetry Based on Multispectral Satellite Imagery and Multibeam Data. *Remote Sensing*, Vol. 7, No. 10, pp. 13782-13806.
- [30] A. Saepuloh et al. 2015. Identifying surface materials on an active volcano by deriving dielectric permittivity from polarimetric SAR data, *IEEE Geoscience and Remote Sensing Letters* **12**(8), 1620-1624.
- [31] A. Freeman, S. L. Durden, 1998. A Three-component scattering model for polarimetric SAR data. *IEEE Transaction Geoscience Remote Sensing*. Vol. 36, No. 3, pp. 963-973.
- [32] N. Demir, M. Kaynarcaa, S. Oya, 2016. Extraction of Coastlines with Fuzzy Approach Using SENTINEL-1 SAR Image. *ISPRS-International Archives of the Photogrammetry, Remote Sensing and Spatial Information Sciences*, Vol. 1, pp. 747-51.
- [33] Z. Liu, F. Li, N. Li, R. Wang, H. Zhang, 2016. A Novel region-merging approach for coastline extraction from Sentinel-1A IW mode SAR imagery. *IEEE Geoscience and Remote Sensing Letters*, Vol. 13, No. 3, pp. 324-328.
- [34] Y. Yamaguchi, T. Moriyama, M. Ishido, H. Yamada, 2005. Four-Component Scattering Model for Polarimetric SAR Image Decomposition. *IEEE Transaction Geoscience Remote Sensing*. Vol. 43, pp. 1699-1706.
- [35] A. Bhattacharya, A. Muhuri, S. De, S. Manickam, A. C. Frery, 2015. Modifying the Yamaguchi four-component decomposition scattering powers using a stochastic distance. *IEEE Journal of Selected Topics in Applied Earth Observations and Remote Sensing*, Vol. 8, No. 7, pp. 3497-3506.
- [36] B. Zou, Y. Zhang, N. Cao, N. P. Minh, 2015. A four-component decomposition model for PolSAR data using asymmetric scattering

component. *IEEE Journal of Selected Topics in Applied Earth Observations and Remote Sensing*, Vol. 8, No. 3, pp. 1051-1061.

[37] Kausarian, H., Sumantyo, J.T.S., Kuze, H., Karya, D. and Panggabean, G.F., 2016. Silica Sand Identification using ALOS PALSAR Full Polarimetry on The Northern Coastline of Rupert Island, Indonesia. *International Journal on Advanced Science, Engineering and Information Technology*, 6(5).

[38] R. W. G. Carter, C. Bill, 2013. *Coastal environments: an introduction to the physical, ecological, and cultural systems of coastlines*. Academic Press, 3rd ed., London.

[39] K. T. Holland et al. 2008. A review of heterogeneous sediments in coastal environments, *Earth-Science Reviews*. **89**(3), 116-134.

[40] W. M. Jeong, H. Cho, W. Baek, 2015. Analysis of the long-term wave characteristics off the coast of Daejin,” *Journal of Korean Society of Coastal and Ocean Engineers*, Vol. 27, No. 2, pp. 142-147.

[41] T. A. Łabuz, 2016. A review of field methods to survey coastal dunes—experience based on research from South Baltic coast. *Journal of Coastal Conservation*, Vol. 20, No. 2, pp. 175-190.

[42] A. E. Dabbagh, K. G. Al-Hinai, M. A. Khan, 1997. Detection of sand-covered geologic features in the Arabian Peninsula using SIR-C/X-SAR data. *Remote Sensing of Environment*, Vol. 59, No. 2, pp.375-382.

7 APPENDICES

LIST OF PUBLICATIONS	82
----------------------	----

LIST OF PUBLICATIONS

Published Journal Papers

1. Kausarian, H, J. T. S. Sumantyo, H. Kuze, A. Jamrud, M. W. Mirza, 2016. Analysis of Backscattering Coefficient and Sample Properties for Identification and Layer Thickness Estimation of Silica Sand Distribution using L-Band Synthetic Aperture Radar: A Case Study on the Northern Coastline of Rupert Island, Indonesia. *Canadian Journal of Remote Sensing*. (Accepted 25 November 2016)
2. Kausarian, H, J. T. S. Sumantyo, H. Kuze, K. Detri, G. F. Panggabean, 2016. Silica Sand Identification using ALOS PALSAR Full Polarimetry on The Northern Coastline of Rupert Island, Indonesia. *International Journal on Advance Science, Engineering and Information Technology (IJASEIT)*. Vol. 6, No. 5, 568-573.

Conference Papers

1. Kausarian, H, J. T. S. Sumantyo, K. Detri, B. E. P. Dewandra, A. K. Evizal, 2016. Geological Mapping for the Land Deformation Using Small UAV, InSAR Analysis and Field Observation at The Siak Bridge I and II, Pekanbaru City, Indonesia. *Indonesia-Japan Joint Scientific Symposium (IJSS) 2016*.
2. Kausarian, H, J. T. S. Sumantyo, H. Kuze, 2016. Identification of Silica Sand Distribution on the northern Coastline of Rupert Island Using ALOS/PALSAR Full Polarimetry Data. *Proceeding International Symposium on Remote Sensing 2016*.
3. Kausarian, H, J. T. S. Sumantyo, H. Kuze, 2015. Physical and dielectric properties measurement to identify the distribution of silica sand using alos/palsar full polarimetry on the northern coastline of rupert island, indonesia. *Proceeding The 23rd CERES International Symposium, Chiba University, Japan*.

4. Kausarian, H, J. T. S Sumantyo, H. Kuze, B. E. P. Dewandra. 2015. Mapping of the oldest layer exposure at the top layer of Riau bedrock using Alos Palsar Mosaic 25M-Resolution data. *Proceeding of The 58th Spring International Conference of the Remote Sensing Society of Japan*. 72-75.